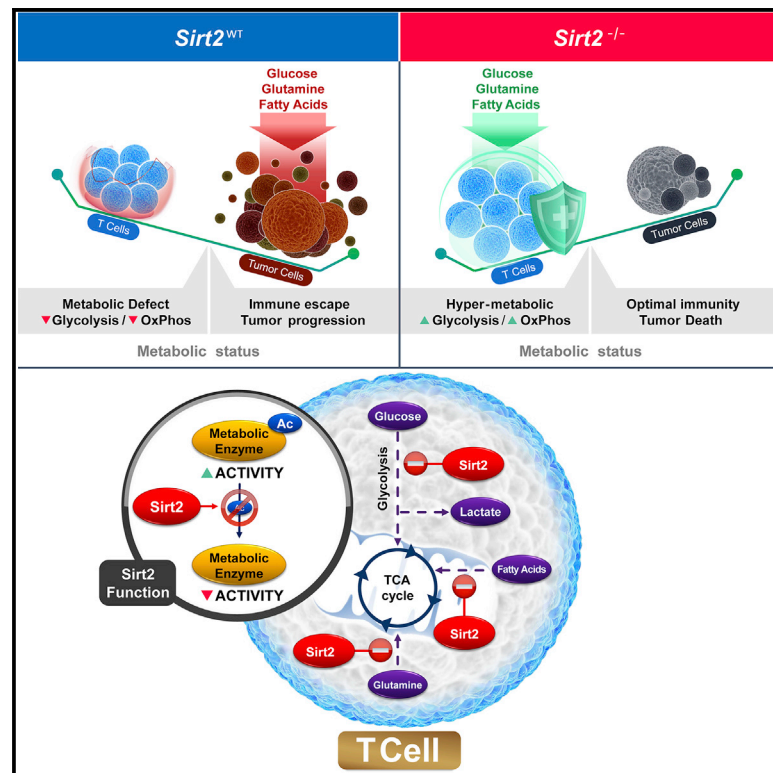


# Cell Metabolism

## Sirt2 Inhibition Enhances Metabolic Fitness and Effector Functions of Tumor-Reactive T Cells

### Graphical Abstract



### Authors

Imene Hamaidi, Lin Zhang, Nayoung Kim, ..., Scott J. Antonia, James J. Mulé, Sungjune Kim

### Correspondence

sungjune.kim@moffitt.org

### In Brief

Hamaidi et al. show that Sirt2 activity governs the metabolic fitness of T cells at the tumor bed by blocking the activity of key metabolic enzymes involved in glycolysis, TCA-cycle, FAO, and glutaminolysis, and thus controls the magnitude of antitumor immune responses.

### Highlights

- Sirt2, an NAD<sup>+</sup>-dependent deacetylase, is overexpressed in TILs
- Sirt2 interaction with key metabolic enzymes regulates T cell metabolism
- Sirt2-deficient T cells exhibit enhanced glycolysis and oxidative phosphorylation
- Sirt2 inhibition enhances effector functions of tumor-reactive T cells

Article

# Sirt2 Inhibition Enhances Metabolic Fitness and Effector Functions of Tumor-Reactive T Cells

Imene Hamaidi,<sup>1</sup> Lin Zhang,<sup>1,9,10</sup> Nayoung Kim,<sup>1,11</sup> Min-Hsuan Wang,<sup>1</sup> Cristina Iclozan,<sup>1</sup> Bin Fang,<sup>2</sup> Min Liu,<sup>2</sup> John M. Koomen,<sup>2,3</sup> Anders E. Berglund,<sup>4</sup> Sean J. Yoder,<sup>5</sup> Jiqiang Yao,<sup>4</sup> Robert W. Engelman,<sup>6</sup> Ben C. Creelan,<sup>7</sup> Jose R. Conejo-Garcia,<sup>1</sup> Scott J. Antonia,<sup>7,12</sup> James J. Mulé,<sup>1</sup> and Sungjune Kim<sup>1,8,13,\*</sup>

<sup>1</sup>Department of Immunology, H. Lee Moffitt Cancer Center, Tampa, FL 33612, USA

<sup>2</sup>Proteomics and Metabolomics Core, H. Lee Moffitt Cancer Center, Tampa, FL 33612, USA

<sup>3</sup>Department of Molecular Oncology, H. Lee Moffitt Cancer Center, Tampa, FL 33612, USA

<sup>4</sup>Department of Biostatistics and Bioinformatics, H. Lee Moffitt Cancer Center, Tampa, FL 33612, USA

<sup>5</sup>Molecular Genomics Core, H. Lee Moffitt Cancer Center, Tampa, FL 33612, USA

<sup>6</sup>Pediatrics, Pathology & Cell Biology, University of South of Florida, Tampa, FL 33612, USA

<sup>7</sup>Department of Thoracic Oncology, H. Lee Moffitt Cancer Center, Tampa, FL 33612, USA

<sup>8</sup>Department of Radiation Oncology, H. Lee Moffitt Cancer Center, Tampa, FL 33612, USA

<sup>9</sup>Present address: Department of Immunology, Tianjin Medical University Cancer Institute and Hospital, Tianjin 300060, China

<sup>10</sup>Present address: Key Laboratory of Cancer Immunology and Biotherapy, Tianjin 300060, China

<sup>11</sup>Present address: Rosetta Exosome Inc, Seoul 140-762, Republic of Korea

<sup>12</sup>Present address: Duke University Medical Center, Durham, NC 27710, USA

<sup>13</sup>Lead Contact

\*Correspondence: [sungjune.kim@moffitt.org](mailto:sungjune.kim@moffitt.org)

<https://doi.org/10.1016/j.cmet.2020.07.008>

## SUMMARY

Dysregulated metabolism is a key driver of maladaptive tumor-reactive T lymphocytes within the tumor micro-environment. Actionable targets that rescue the effector activity of antitumor T cells remain elusive. Here, we report that the Sirtuin-2 (Sirt2) NAD<sup>+</sup>-dependent deacetylase inhibits T cell metabolism and impairs T cell effector functions. Remarkably, upregulation of Sirt2 in human tumor-infiltrating lymphocytes (TILs) negatively correlates with response to TIL therapy in advanced non-small-cell lung cancer. Mechanistically, Sirt2 suppresses T cell metabolism by targeting key enzymes involved in glycolysis, tricarboxylic acid-cycle, fatty acid oxidation, and glutaminolysis. Accordingly, Sirt2-deficient murine T cells exhibit increased glycolysis and oxidative phosphorylation, resulting in enhanced proliferation and effector functions and subsequently exhibiting superior antitumor activity. Importantly, pharmacologic inhibition of Sirt2 endows human TILs with these superior metabolic fitness and effector functions. Our findings unveil Sirt2 as an unexpected actionable target for reprogramming T cell metabolism to augment a broad spectrum of cancer immunotherapies.

## INTRODUCTION

Despite unprecedented success with cancer immunotherapy, a majority of patients remain refractory to the treatment (Pardoll, 2012). The clinical efficacy of tumor-reactive tumor-infiltrating

lymphocyte (TIL) therapy is limited by the loss of T cell effector functions within the tumor microenvironment (TME) (Rosenberg and Restifo, 2015). There is a growing evidence that metabolic fitness of T cells determines their function and fate (Karmaus et al., 2019; Zhao et al., 2016), and its restriction by nutrient

### Context and Significance

Metabolic fitness is a key driver of T cell functions, and dysregulated metabolism contributes to the loss of their effector functions within the nutrient-restricted TME. Researchers at the H. Lee Moffitt Cancer Center and their colleagues identified Sirt2, an NAD<sup>+</sup>-dependent protein deacetylase, as a master metabolic immune checkpoint that negatively regulates T cell metabolism through targeting key metabolic enzymes. This study shows that Sirt2 overexpression in TILs correlates with a poor clinical response to TIL therapy in patients with advanced NSCLC. Accordingly, Sirt2 inhibition reprograms T cell metabolism to optimally engage aerobic glycolysis and mitochondrial respiration to sustain T cell effector function within the metabolically challenging TME, leading to an effective antitumor immune response.

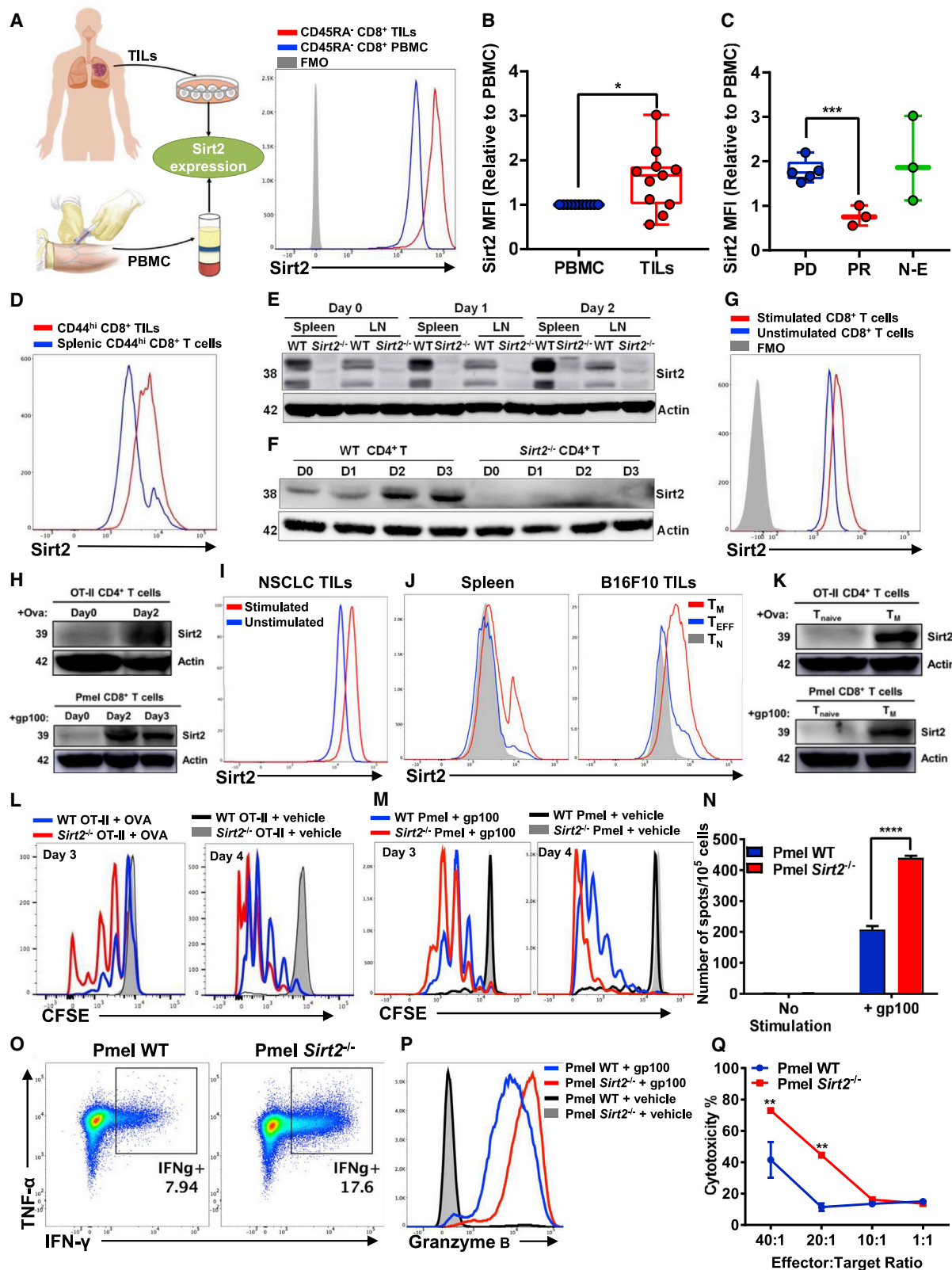


**Figure 1. Sirt2 Expression Is Induced upon Activation and within the TME and Its Deficiency Promotes T Cell Hyper-Reactivity**

(A) Sirt2 expression levels in human CD45RA<sup>-</sup> CD8<sup>+</sup> TILs versus PBMC by flow cytometry (n = 11).

(B) Sirt2 expression levels in human CD45RA<sup>-</sup> CD8<sup>+</sup> TILs normalized to the corresponding CD45RA<sup>-</sup> CD8<sup>+</sup> PBMC and plotted as shown.

(legend continued on next page)

competition from tumor cells contributes to immune escape (Chang et al., 2015). Thus, new strategies are needed to overcome the immune suppressive TME, and hence, metabolic manipulation of T cells to optimally compete with cancer cells is an attractive strategy.

Naive T ( $T_N$ ) cells are relatively quiescent and rely on oxidative phosphorylation (OxPhos) to generate ATP from glucose or fatty acids (FA) (Chang et al., 2013). Following antigenic stimulation, there is a switch toward a larger reliance on aerobic glycolysis, which provides the necessary intermediates for rapid proliferation and specialized effector functions (Chang et al., 2013; Lunt and Vander Heiden, 2011). Glutamine uptake and glutaminolysis are also upregulated in activated T cells (Johnson et al., 2018). Memory T ( $T_M$ ) cells adopt the metabolic phenotype of non-proliferative cells, predominantly utilizing OxPhos fueled by FA oxidation (FAO) (Pearce et al., 2013). This catabolic pathway is also critical for TILs under metabolic stress within the hypoglycemic and hypoxic TME (Zhang et al., 2017).

Protein acetylation has emerged as a key post-translational modification in cell metabolism, as virtually every glycolytic and tricarboxylic acid (TCA)-cycle enzyme undergoes acetylation (Zhao et al., 2010); yet, the relevance of these modifications to the immune metabolism has not been explored. Histone deacetylase class III proteins, also termed as Sirtuins, are nicotinamide adenine dinucleotide ( $NAD^+$ )-dependent deacetylases. In mammals, there are seven Sirtuins (Sirt1–7) with distinct subcellular localization and functions (Guarente, 2011; Houtkooper et al., 2012). Sirt1, Sirt6, and Sirt7 are localized in the nucleus, where they deacetylate histones. Sirt3–5 are localized in mitochondria, where they modulate the oxidative stress and ATP production in response to caloric restriction (Verdin et al., 2010).

Sirtuin-2 (Sirt2) is predominantly cytosolic, co-localizes with microtubules, and deacetylates  $\alpha$ -tubulin (North et al., 2003). Sirt2 has received a considerable attention as a regulator of aging and is induced following caloric restriction and oxidative stress (Gomes et al., 2015). In cancer, Sirt2 has been paradoxically reported to have tumor-suppressor and oncogenic functions (Jing et al., 2016; McGlynn et al., 2014). In the immune system, Sirt2 suppresses inflammation via negative regulation of nuclear factor- $\kappa$ B (NF- $\kappa$ B) p65 subunit (Rothgiesser et al., 2010). Accordingly, Sirt2-deficient mice develop severe forms of dextran sodium sulfate-induced colitis via polarization of pro-inflammatory

macrophages (Lo Sasso et al., 2014). However, the role of Sirt2 in T cell metabolism and tumor immunity has not been described.

Here, we report that upregulation of Sirt2 expression in human TILs correlates with poor clinical response to immunotherapy, and Sirt2 deficiency leads to hyper-reactive T cells with superior antitumor activity. Mechanistically, Sirt2 loss or inhibition during T cell activation provokes hyper-acetylation of multiple metabolic enzymes and amplification of their activities, leading to increased aerobic glycolysis and OxPhos. In conclusion, this superior metabolic phenotype of Sirt2 inhibition allows T cells to overcome the immune and metabolic barrier within the suppressive TME and thus augments tumor immunity.

## RESULTS

### Sirt2 Expression Is Upregulated during T Cell Activation, Maturation, and within the TME

To gain an insight into the role of Sirt2 in tumor immunity, human peripheral blood mononuclear cells (PBMC) and matching TILs from 11 patients enrolled into a phase I clinical trial of Nivolumab and TIL therapy in advanced non-small cell lung cancer (NSCLC) (Creelan et al., 2018) were analyzed for Sirt2 expression. Overall,  $CD8^+ CD45RA^-$  TILs demonstrated a significant increase in Sirt2 expression when compared with the corresponding peripheral  $CD8^+ CD45RA^-$  T cells (Figures 1A and 1B). However, Sirt2 upregulation in TILs versus PBMC was not observed in 3 patients who achieved partial response to the TIL therapy. Conversely, 6 non-responder patients exhibited a significant upregulation of Sirt2 levels in TILs versus PBMC (Figure 1C). These findings were recapitulated in preclinical models *in vivo*, whereby Sirt2 expression was upregulated in  $CD44^{high} CD8^+$  TILs isolated from subcutaneous (s.c.) B16F10 nodules versus splenic  $CD44^{high} CD8^+$  T cells (Figure 1D).

Interestingly, we found that Sirt2 expression was induced following T cell receptor (TCR) stimulation with either CD3 ligation in T cells from C57BL/6 mice or cognate antigenic peptides in OT-II (OVA<sub>323–339</sub>) or Pmel (gp100<sub>25–33</sub>) T cells (Figures 1E–1H). Consistently, Sirt2 expression was upregulated following CD3 ligation in human TILs from NSCLC patients (Figure 1I). In contrast, Sirt2 expression remained unchanged following cytokine stimulation (Figure S1A).

(C) Sirt2 expression levels in human TILs were correlated to the clinical response to immunotherapy. PD, progressive disease; PR, partial response; N-E, Non-evaluable.

(D) Sirt2 expression levels in  $CD44^{high} CD8^+$  TILs versus splenic T cells by flow cytometry ( $n = 3$ ).

(E and F) WB of Sirt2 protein levels in WT versus Sirt2<sup>-/-</sup> T cells from spleen and lymph node (LN) (E), and  $CD4^+$  T cells (F), at day 0 and 1–3 days post CD3 stimulation.

(G) Sirt2 expression levels in naive versus activated  $CD8^+$  T cells by flow cytometry ( $n = 2$ ).

(H) WB of Sirt2 protein levels in naive versus activated  $CD4^+$  OT-II (upper panel) and  $CD8^+$  Pmel (lower panel) T cells.

(I) Sirt2 expression levels in non-stimulated and CD3-stimulated human  $CD8^+$  TILs by flow cytometry ( $n = 4$ ).

(J) Sirt2 expression levels in  $CD8^+ T_N$ ,  $T_{EFF}$ , and  $T_M$  cell subsets of spleen (left panel) and TILs (right panel) by flow cytometry ( $n = 3$ ).

(K) WB of Sirt2 protein levels in  $CD4^+$  OT-II (upper panel) and  $CD8^+$  Pmel (lower panel)  $T_N$  versus  $T_M$  cells.

(L and M) Proliferation of carboxyl fluorescein succinimidyl ester (CFSE)-labeled WT versus Sirt2<sup>-/-</sup> OT-II (L) and Pmel (M) T cells ( $n = 7$ ).

(N–Q) Functional characterization of WT versus Sirt2<sup>-/-</sup> Pmel T cells. (N) IFN- $\gamma$  ELISPOT assay was performed ( $n = 4$ ). (O) TNF- $\alpha$  and IFN- $\gamma$  expression levels by flow cytometry ( $n = 7$ ). (P) Granzyme B expression levels by flow cytometry ( $n = 7$ ). (Q) Cytotoxic activities of WT versus Sirt2<sup>-/-</sup> Pmel  $CD8^+$  T cells after co-culture with B16F10 cells ( $n = 3$ ).

(A) and (G) FMO, fluorescence minus one control. (E), (F), (H), and (K) Actin levels were used as loading control.

Data are mean  $\pm$  standard error of the mean (SEM). \* $p < 0.05$ , \*\* $p < 0.01$ , \*\*\* $p < 0.001$ , \*\*\*\* $p < 0.0001$ .

See also Figure S1.

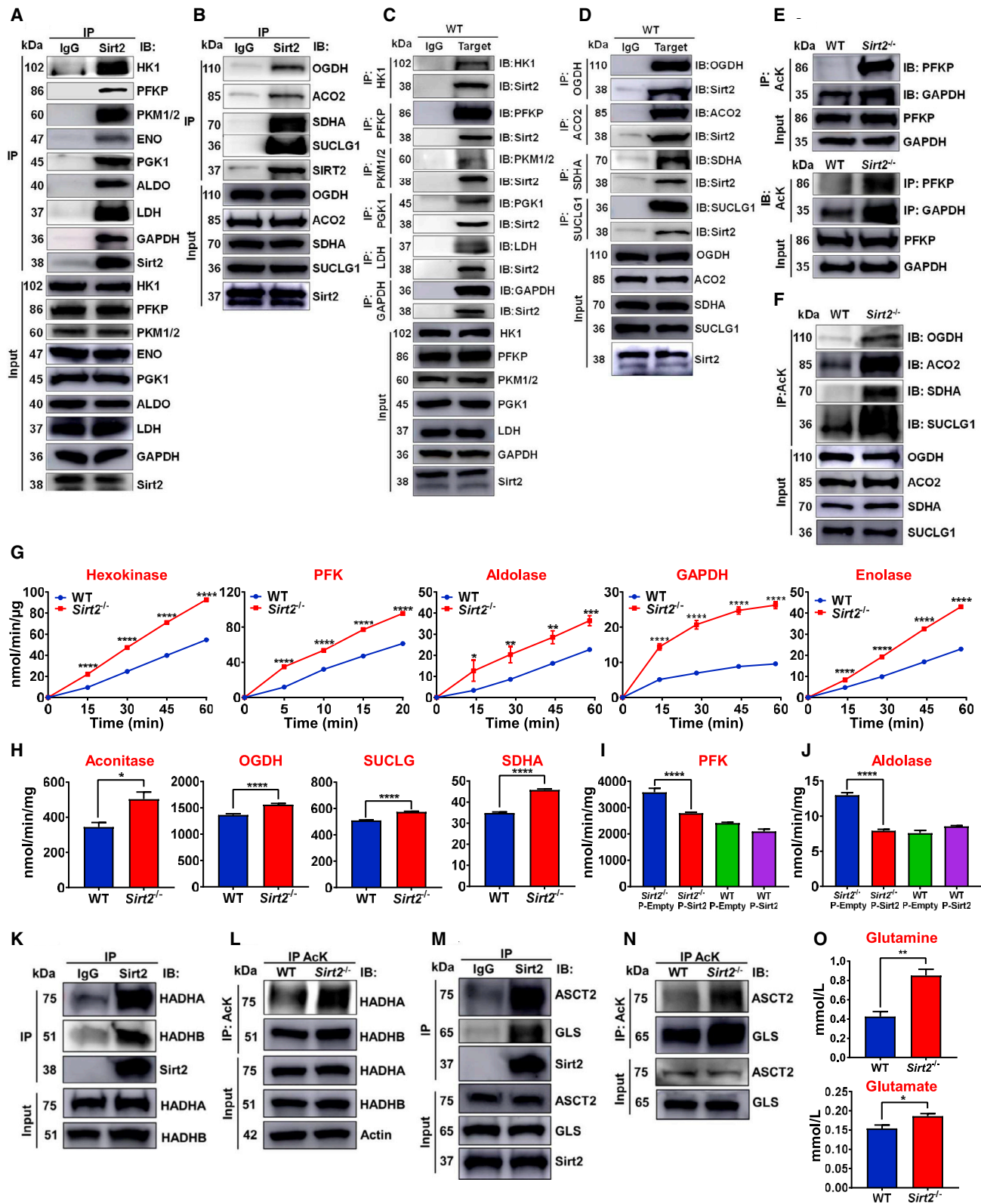


**Figure 2. Sirt2 Directly Interacts with Key Enzymes of Glycolysis, TCA-Cycle, FAO, and Glutaminolysis**

(A and B) CoIP of HK1, PFKP, PKM1/2, ENO, PGK1, Aldo, LDH, GAPDH from the glycolytic pathway (A) and OGDH, ACO2, SDHA, SUCLG1 from the TCA-cycle (B) by anti-Sirt2 on CD3<sup>+</sup> T cells.

(legend continued on next page)

Strikingly, Sirt2 was differentially expressed among T cell subsets, prominently upregulated in  $T_M$  cells in spleen and within the TME (Figure 1J). Upregulation of Sirt2 expression in  $T_M$  cells was confirmed by western blot (WB) on IL-15 differentiated OT-II and Pmel  $T_M$  cells *ex vivo* (Figure 1K). Thus, Sirt2 expression is dynamically regulated during T cell activation, maturation, and within the TME.

### Sirt2-Deficient T Cells Are Hyper-Reactive

Since Sirt2 expression is induced upon TCR stimulation, we then investigated how Sirt2 contributes to T cell functions. We found that Sirt2-knockout (Sirt2<sup>-/-</sup>) in OT-II and Pmel T cells exhibited increased proliferation following antigenic stimulation compared with their Sirt2-wild-type (WT) counterparts (Figures 1L and 1M). Corresponding increases in IFN- $\gamma$  production and granzyme B expression were manifested in activated Sirt2<sup>-/-</sup> Pmel T cells (Figures 1N–1P). Enhanced reactivity of Sirt2<sup>-/-</sup> Pmel T cells led to increased cytotoxic activity against B16F10 cells *ex vivo* (Figure 1Q).

Moreover, RNA-sequencing (RNA-seq) analysis revealed more than 800 differentially expressed genes between activated WT and Sirt2<sup>-/-</sup> CD4<sup>+</sup> T cells (Figure S1B). Interestingly, the pathway enrichment analysis showed upregulation of pathways related to T cell effector function and proliferation with Sirt2 deficiency, including IFN- $\gamma$  response and IL-2 signaling (Figure S1C). Therefore, Sirt2 upregulation limits the proliferative capacity and effector activity of antigen-stimulated T cells.

We next investigated whether Sirt2<sup>-/-</sup> phenotype is influenced by compensatory changes in other Sirtuins with known immune functions. RNA-seq analysis did not reveal significant changes in Sirt1–7 expression levels between WT and Sirt2<sup>-/-</sup> T cells (Figure S1D), which was confirmed by WB (Figure S1E). These results suggest that the role of Sirt2 in T cells is independent of other Sirtuin family members.

### Sirt2 Targets the Glycolytic and TCA Pathways in T Cells

To gain an insight into the molecular mechanism underlying the hyper-reactivity of Sirt2<sup>-/-</sup> T cells, we sought to identify Sirt2 partners that regulate T cell functions.

First, we performed liquid chromatography-tandem mass spectrometry (LC-MS/MS) analysis on Sirt2-immunoprecipitated proteins from CD3<sup>+</sup> T cells. Notably, among the ten glycolytic enzymes, eight were identified as Sirt2 interacting proteins, including hexokinase 1 (HK1), phosphofructokinase P (PFKP), aldolase A (ALDOA), glyceraldehyde-3-phosphate dehydroge-

nase (GAPDH), phosphoglycerate kinase 1 (PGK1), enolase 1 (ENO1), pyruvate kinase M (PKM), and lactate dehydrogenase (LDH) (Figure S2A). In addition, among the eight TCA-cycle enzymes, aconitase 2 (ACO2), oxoglutarate dehydrogenase (OGDH), succinate-CoA ligase alpha subunit (SUCLG1), and succinate dehydrogenase subunit alpha (SDHA) were also identified as binding Sirt2 (Figure S2B). These interactions were confirmed by co-immunoprecipitation-immunoblot (coIP-IB) (Figures 2A–2D).

Second, we performed LC-MS/MS analysis on acetyl-lysine (AcK)-immunoprecipitated proteins from WT versus Sirt2<sup>-/-</sup> CD3<sup>+</sup> T cells. More than 250 hyper-acetylated proteins were identified in Sirt2<sup>-/-</sup> T cells. Based on the extracted ion chromatogram (EIC), differentially acetylated proteins included ALDOA, HK1, GAPDH, PGK1, ENO1, PKM, and LDH from the glycolytic pathway and ACO2, isocitrate dehydrogenase (IDH), SUCLG1, SDHA, and malate dehydrogenase (MDH) from the TCA-cycle (Figure S2C). Increased acetylation of PFK, GAPDH, ACO2, OGDH, SDHA, and SUCLG1 in Sirt2<sup>-/-</sup> versus WT T cells was confirmed by IP-IB (Figures 2E and 2F).

Supporting the functional relevance of the altered acetylation of glycolytic and TCA-cycle enzymes, enzymatic activities of HK, PFK, ALDO, GAPDH, ENO, ACO, OGDH, SDH, and SUCLG were all elevated in activated Sirt2<sup>-/-</sup> T cells versus WT T cells (Figures 2G and 2H), despite no visible differences in their total protein levels (Figures S2D and S2E). Importantly, enhanced PFK and ALDO activities in activated Sirt2<sup>-/-</sup> T cells were reversed when Sirt2 expression was restored (Figures 2I and 2J). Taken together, these results demonstrate Sirt2 interaction with key enzymes of the glycolytic pathway and the TCA cycle.

### Sirt2 Targets FAO and Glutaminolysis Pathways in T Cells

The trifunctional protein (TFP) that catalyzes the last three reactions of FAO has two subunits: hydroxyacyl-CoA dehydrogenase trifunctional multienzyme complex subunits alpha (HADHA) and beta (HADHB) (Figure S3A). Interestingly, our LC-MS/MS analyses revealed HADHA and HADHB as Sirt2 interacting partners (Figure S3A) with hyper-acetylation of HADHB in Sirt2<sup>-/-</sup> T cells (Figure S3B). These interactions were confirmed by coIP-IB (Figure 2K). IP-IB also demonstrated hyper-acetylation of HADHA and HADHB subunits in Sirt2<sup>-/-</sup> versus WT T cells (Figure 2L), while their total proteins were unchanged (Figure S3C).

Glutamine enters cells using the alanine, serine, cysteine-preferring transporter 2 (ASCT2), and it is converted to glutamate

(C and D) CoIP of Sirt2 by anti-HK1, anti-PKM1/2, anti-PGK1, anti-LDH, anti-GAPDH from the glycolytic pathway (C) and anti-OGDH, anti-ACO2, anti-SDHA, anti-SUCLG1 from the TCA-cycle (D) on CD3<sup>+</sup> T cells.

(E and F) Determination of acetylation levels of GAPDH, PFKP from the glycolytic pathway (E) and OGDH, ACO2 SDHA, SUCLG1 from the TCA-cycle (F) on WT versus Sirt2<sup>-/-</sup> CD3<sup>+</sup> T cells.

(G and H) Enzymatic activities of aldolase (n = 5), enolase (n = 4), GAPDH (n = 5), PFK (n = 5), hexokinase (n = 6) from the glycolytic pathway (G), and aconitase (n = 3), SUCLG (n = 6), SDH (n = 8), OGDH (n = 6) from the TCA-cycle (H).

(I and J) Enzymatic activities of PFK (n = 6) (I), and aldolase (n = 3–6) (J), were assessed from WT versus Sirt2<sup>-/-</sup> T cells transduced with P-Sirt2 or P-empty lentivectors.

(K and M) CoIP of HADHA and HADHB from FAO (K), and ASCT2, GLS from glutaminolysis (M) by anti-Sirt2 on CD3<sup>+</sup> T cells.

(L and N) Determination of acetylation levels of HADHA and HADHB from FAO (L), and ASCT2 and GLS from glutaminolysis (N) on WT versus Sirt2<sup>-/-</sup> CD3<sup>+</sup> T cells.

(A)–(F) and (K)–(N) WB of each target using equal amounts of total protein extracts is shown as the input control for IP.

(O) Glutamine consumption (upper panel) and glutamate production (lower panel) (n = 3).

Data are mean  $\pm$  SEM. \*p < 0.05, \*\*p < 0.01, \*\*\*p < 0.001, \*\*\*\*p < 0.0001.

See also Figures S2 and S3.

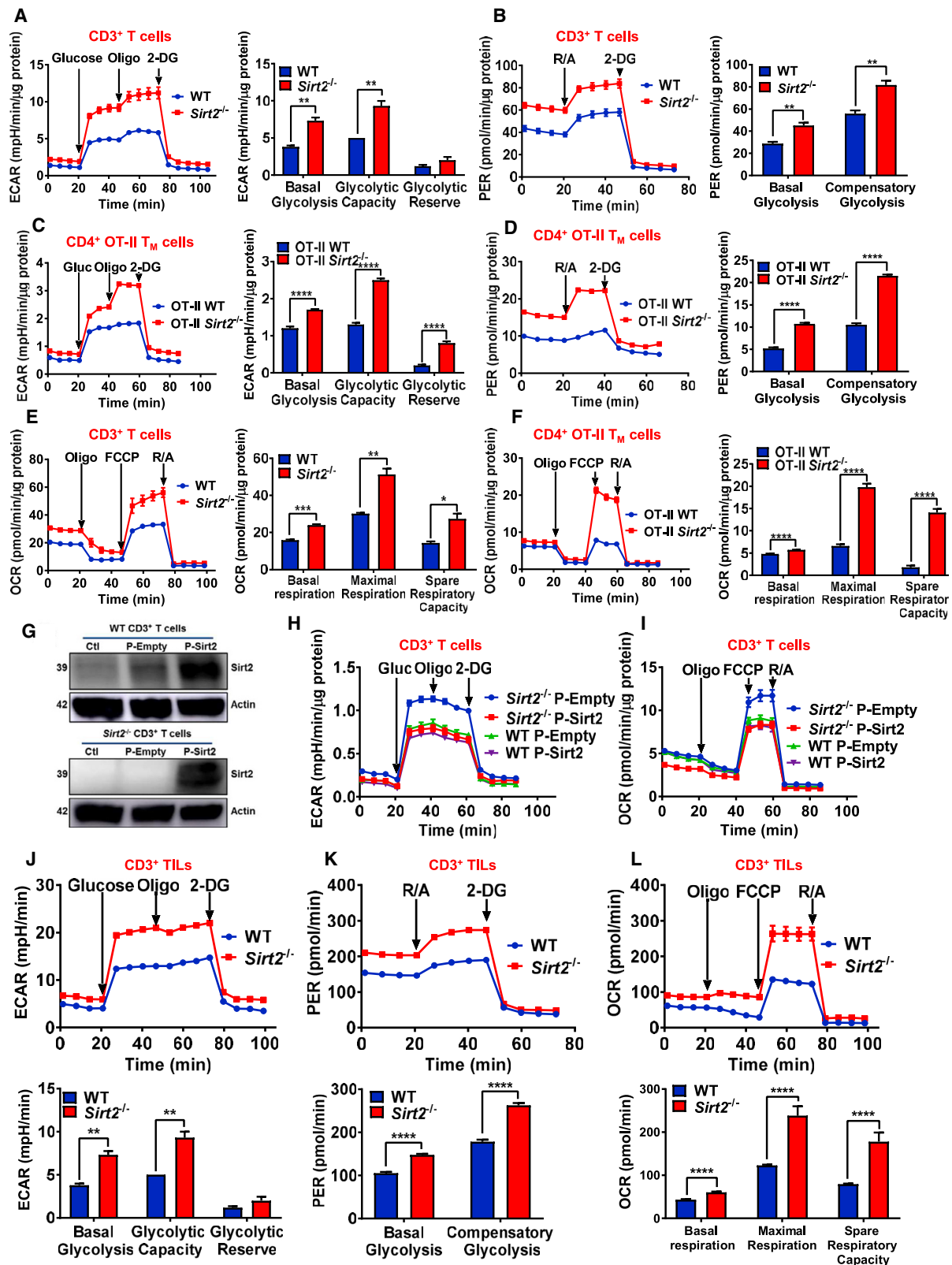


**Figure 3. Glycolysis and OxPhos Are Increased in Sirt2<sup>-/-</sup> T Cells**

(A and C) Left, Extracellular acidification rate (ECAR) of activated WT (n = 3) versus Sirt2<sup>-/-</sup> (n = 3) CD3<sup>+</sup> T cells (A); and WT (n = 16) versus Sirt2<sup>-/-</sup> (n = 16) CD4<sup>+</sup> OT-II T<sub>M</sub> cells (C). Glucose, Oligo, and 2-DG were injected at the indicated time points. Right, basal glycolytic rate, glycolytic capacity, and glycolytic reserve.

(legend continued on next page)

by glutaminase (GLS) and to  $\alpha$ -ketoglutarate ( $\alpha$ -KG) by glutamate dehydrogenase (GDH) (Figure S3D). Our LC-MS/MS analyses revealed ASCT2 interaction with Sirt2 (Figure S3D) and increased acetylation of GLS and GDH in Sirt2<sup>-/-</sup> T cells (Figure S3E). We, therefore, confirmed Sirt2 interaction with ASCT2 and GLS by coIP-IB (Figure 2M). We also demonstrated hyper-acetylation of ASCT2 and GLS in Sirt2<sup>-/-</sup> versus WT T cells by IP-IB (Figure 2N). To address whether the acetylation level of these enzymes affects their activity, we measured glutamine consumption and glutamate production in activated WT versus Sirt2<sup>-/-</sup> CD3<sup>+</sup> T cells. As expected, Sirt2<sup>-/-</sup> T cells showed a significant increase in both glutamine uptake and glutamate production (Figure 2O), while no differences in ASCT2 and GLS protein levels were observed between WT and Sirt2<sup>-/-</sup> T cells (Figure S3F). These results suggest a potential role of Sirt2 in FAO and glutaminolysis pathways in activated T cells.

### Sirt2<sup>-/-</sup> T Cells Exhibit Enhanced Glycolysis and OxPhos

Given that Sirt2 interacts with and modifies the acetylation status of multiple metabolic enzymes, we assessed whether Sirt2<sup>-/-</sup> T cells displayed altered metabolic activity during activation and maturation.

Confirming the functional relevance of Sirt2 activity, Sirt2 deficiency increased the glycolytic flux of activated CD3<sup>+</sup>, CD8<sup>+</sup>, and Pmel CD8<sup>+</sup> T cells (Figures 3A, 3B, and S4A–S4D), as well as IL-15 differentiated CD4<sup>+</sup> OT-II and CD8<sup>+</sup> Pmel T<sub>M</sub> cells (Figures 3C, 3D, S4E, and S4F). Likewise, activated Sirt2<sup>-/-</sup> CD3<sup>+</sup>, CD8<sup>+</sup> T cells and IL-15 differentiated CD4<sup>+</sup> OT-II, and CD8<sup>+</sup> Pmel T<sub>M</sub> cells displayed increased mitochondrial activity (Figures 3E, 3F, S4G, and S4H). Importantly, rescuing Sirt2 expression in activated Sirt2<sup>-/-</sup> T cells decreased their glycolytic flux and mitochondrial activity to the levels observed in WT T cells (Figures 3G–3I). Moreover, Sirt2<sup>-/-</sup> TILs isolated from s.c. B16F10 tumors displayed increased glycolysis and OxPhos compared with WT TILs, confirming the role of Sirt2 within the metabolically restricted TME (Figures 3J–3L).

To investigate whether Sirt2<sup>-/-</sup> T cell hyper-reactivity is dependent on their increased metabolic activity, T cells were treated with the glycolytic inhibitor 2-deoxyglucose (2-DG) or the OxPhos inhibitor, oligomycin (Oligo) (Figure 4A). As predicted, 2-DG and Oligo treatments profoundly suppressed IFN- $\gamma$  release (Figures 4B and 4C) and cytotoxicity (Figures 4D

and 4E) by Sirt2<sup>-/-</sup> Pmel T cells to the levels exhibited by WT Pmel T cells. Similarly, 2-DG suppressed IFN- $\gamma$  release by Sirt2<sup>-/-</sup> CD3<sup>+</sup> TILs to the levels exhibited by WT TILs (Figure 4F). These results suggest that the hyper-reactivity of Sirt2<sup>-/-</sup> T cells is associated with their hyper-metabolic phenotype.

Next, we determined the primary mitochondrial fuel mediating enhanced OxPhos in Sirt2<sup>-/-</sup> T cells by subjecting T cells to the selective metabolic inhibitors: UK5099, a pyruvate carrier inhibitor; BPTES, a GLS inhibitor; and etomoxir, a carnitine palmitoyl transferase 1A (CPT1 $\alpha$ ) inhibitor (Figure 4G). In activated WT CD3<sup>+</sup> T cells, the maximal respiration in response to Carbonyl cyanide-p-trifluoromethoxyphenylhydrazone (FCCP) was significantly suppressed by all three inhibitors (UK5099 > BPTES > etomoxir), indicating that proliferating T cells use pyruvate, glutamine, and FA to fuel OxPhos with a preference for pyruvate (Figure 4H, upper panel). Interestingly, Sirt2<sup>-/-</sup> T cells were insensitive to the same inhibitors (Figure 4H, lower panel), which may reflect a superior capacity for glycolysis, glutaminolysis, and FAO.

Given that activated Sirt2<sup>-/-</sup> T cells exhibit increased spare respiratory capacity with an enhanced capacity to utilize pyruvate, glutamine, and FA to fuel the mitochondrial activity, we examined the mitochondria of WT versus Sirt2<sup>-/-</sup> CD4<sup>+</sup> OT-II T cells. Transmission electron microscopy (TEM) did not show significant differences in the mitochondrial density and morphology between Sirt2<sup>-/-</sup> and WT OT-II T cells (Figures S4I and S4J). MitoTracker green staining showed similar results (Figure S4K), suggesting that an enhanced OxPhos in Sirt2<sup>-/-</sup> T cells is unrelated to mitochondrial biogenesis and rather depends on increased mitochondrial enzymatic activities via their post-translational regulation.

Together, these results indicate that Sirt2 activity restrains aerobic glycolysis and OxPhos during T cell activation and maturation.

### Sirt2 Deficiency Enhances FAO and Supports TIL and T<sub>M</sub> Cell Persistence

TILs rely on FA catabolism to preserve their effector functions due to nutrient competition for glucose and glutamine with tumor cells (Zhang et al., 2017). Accordingly, we investigated the contribution of FA in the mitochondrial activity of TILs isolated from s.c. B16F10 nodules. Interestingly, physiologic levels of etomoxir decreased the maximal respiration of WT TILs,

(B and D) Left, proton efflux rate (PER) of activated WT (n = 4) versus Sirt2<sup>-/-</sup> (n = 4) CD3<sup>+</sup> T cells (B); and WT (n = 16) versus Sirt2<sup>-/-</sup> (n = 14) CD4<sup>+</sup> OT-II T<sub>M</sub> cells (D). Rotenone/Antimycin A (R/A) and 2-DG were injected at the indicated time points. Right, basal glycolytic rate, and compensatory glycolysis. (E and F) Left, oxygen consumption rate (OCR) of activated WT (n = 3) versus Sirt2<sup>-/-</sup> (n = 3) CD3<sup>+</sup> T cells (E); and WT (n = 14) versus Sirt2<sup>-/-</sup> (n = 16) CD4<sup>+</sup> OT-II T<sub>M</sub> cells (F). Oligo, FCCP, and R/A were injected at the indicated time points. Right, basal respiration, maximal respiration, and spare respiratory capacity. (G) WB of Sirt2 protein levels in WT versus Sirt2<sup>-/-</sup> CD3<sup>+</sup> T cells transduced with P-Sirt2 or P-empty lentivectors. Actin levels were used as loading control. (H) ECAR of WT versus Sirt2<sup>-/-</sup> CD3<sup>+</sup> T cells transduced with P-Sirt2 or P-empty lentivectors. Glucose, Oligo, and 2-DG were injected at the indicated time points. WT P-Empty (n = 10); WT P-Sirt2 (n = 14); Sirt2<sup>-/-</sup> P-Empty (n = 15); Sirt2<sup>-/-</sup> P-Sirt2 (n = 14). (I) OCR of WT versus Sirt2<sup>-/-</sup> CD3<sup>+</sup> T cells transduced with P-Sirt2 or P-empty lentivectors. Oligo, FCCP, and R/A were injected at the indicated time points. WT P-Empty (n = 4); WT P-Sirt2 (n = 7); Sirt2<sup>-/-</sup> P-Empty (n = 6); Sirt2<sup>-/-</sup> P-Sirt2 (n = 6). (J) Upper, ECAR of WT (n = 13) versus Sirt2<sup>-/-</sup> (n = 7) CD3<sup>+</sup> TILs. Glucose, Oligo, and 2-DG were injected at the indicated time points. Lower, basal glycolytic rate, glycolytic capacity, and glycolytic reserve. (K) Upper, PER of WT (n = 11) versus Sirt2<sup>-/-</sup> (n = 6) CD3<sup>+</sup> TILs. R/A and 2-DG were injected at the indicated time points. Lower, basal glycolytic rate and compensatory glycolysis. (L) Upper, OCR of WT (n = 11) versus Sirt2<sup>-/-</sup> (n = 8) CD3<sup>+</sup> TILs. Oligo, FCCP, and R/A were injected at the indicated time points. Lower, basal respiration, maximal respiration, and spare respiratory capacity. Data are mean  $\pm$  SEM. \*p < 0.05, \*\*p < 0.01, \*\*\*p < 0.001, \*\*\*\*p < 0.0001. See also Figure S4.

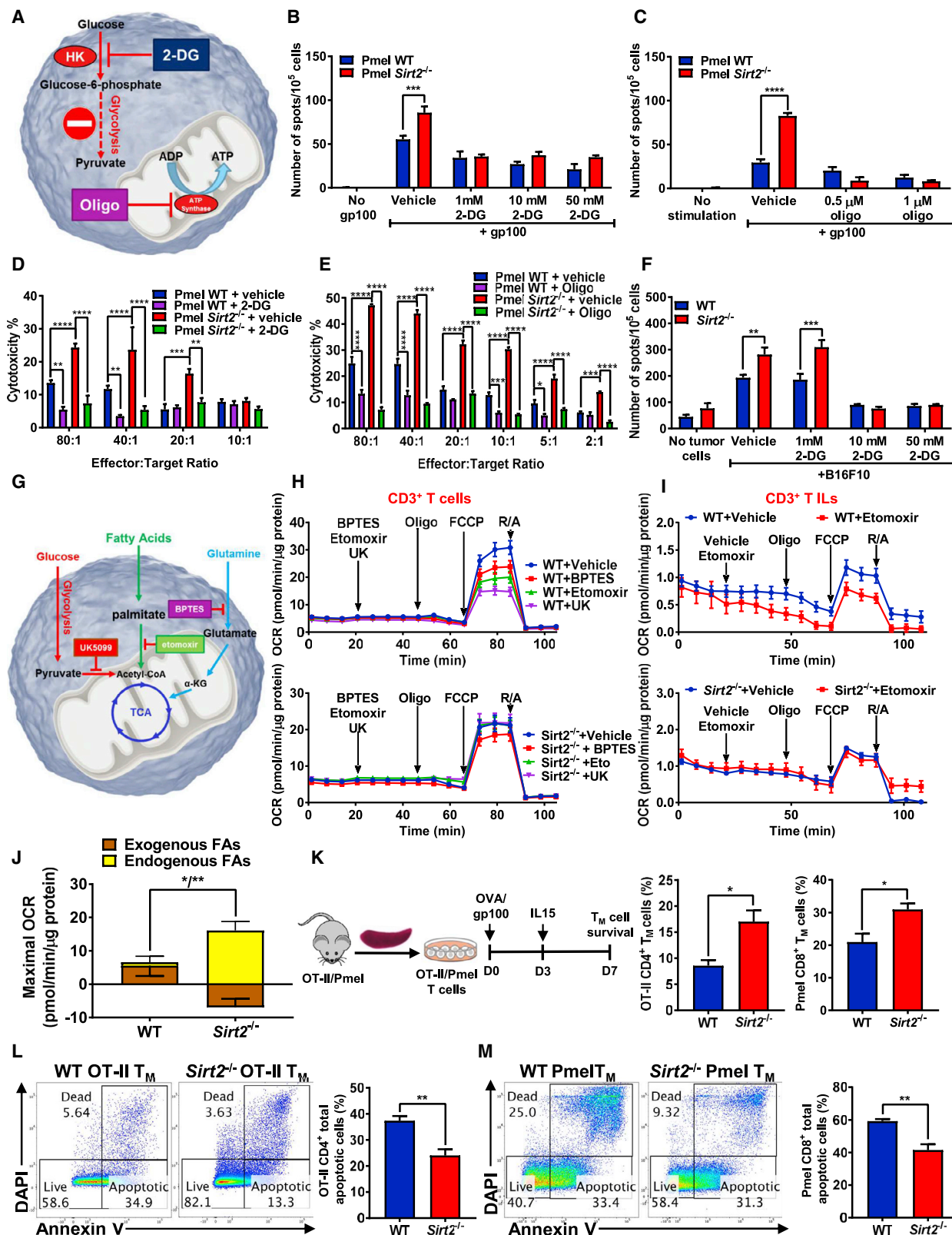


**Figure 4. *Sirt2*<sup>-/-</sup> T Cell Hyper-Reactivity Depends on Glycolysis and OxPhos, and *Sirt2*<sup>-/-</sup> T<sub>M</sub> Cell Accumulation Depends on FAO**

(A) The schematic shows 2-DG and Oligo targets.

(B and C) IFN- $\gamma$  ELISPOT assay on WT versus *Sirt2*<sup>-/-</sup> Pmel T cells treated with the indicated concentrations of 2-DG (B), and Oligo (C) (n = 3).

(legend continued on next page)

whereas Sirt2<sup>-/-</sup> TILs remained resistant to etomoxir inhibition (Figure 4I).

Long-lived T<sub>M</sub> cells rely on FAO for survival and utilize endogenously synthesized FA substrates to support their OxPhos (O'Sullivan et al., 2014; van der Windt et al., 2013). We, therefore, investigated whether enhanced FAO in activated Sirt2<sup>-/-</sup> T cells is dependent on exogenous or endogenous FAs. Interestingly, Sirt2<sup>-/-</sup> T cells challenged with restricted media displayed higher oxidation of endogenous FAs than exogenous FAs when compared with WT T cells (Figure 4J). Further, consistent with enhanced FAO, increased accumulation of Sirt2<sup>-/-</sup> CD4<sup>+</sup> OT-II and Sirt2<sup>-/-</sup> CD8<sup>+</sup> Pmel T<sub>M</sub> cells was manifested (Figure 4K), which was associated with decreased apoptosis when compared with WT T<sub>M</sub> cells (Figures 4L and 4M).

### Sirt2 Is a Master Organizer of T Cell Metabolism

C-Myc and the mammalian target of rapamycin complex 1 (mTORC1)-hypoxia-inducible factor 1 alpha (HIF-1 $\alpha$ ) signaling are important regulators of the T cell metabolism (He et al., 2018; Wang et al., 2011). However, gene expression profiling did not reveal any significant increase in c-Myc-dependent transcriptome (Figure S5A) or mTORC1-HIF-1 $\alpha$  signaling between WT and Sirt2<sup>-/-</sup> T cells (Figure S1C). Similarly, Wb analysis showed no differences in c-Myc, HIF-1 $\alpha$ , and the phospho-S6 ribosomal protein (P-S6, mTOR downstream target) expression levels between WT and Sirt2<sup>-/-</sup> T cells (Figures S5B and S5C). These results confirm that the hyper-metabolic phenotype of Sirt2<sup>-/-</sup> T cells is mediated through a post-translational control of T cell metabolism and is not dependent on the transcriptional control by c-Myc and mTORC1-HIF-1 $\alpha$ .

To corroborate the hyper-metabolic phenotype of Sirt2<sup>-/-</sup> T cells, we performed untargeted metabolomic LC/MS analysis of intracellular metabolites in activated WT versus Sirt2<sup>-/-</sup> CD8<sup>+</sup> T cells (Figures 5A and 5B). Metabolites set enrichment analysis indicated upregulation of multiple metabolic pathways in Sirt2<sup>-/-</sup> T cells, most notably the Warburg effect, FA, and glutamine metabolisms (Figure 5C). Indeed, Sirt2<sup>-/-</sup> T cells showed a significant drop in glucose and an increase in glucose-6-phosphate levels (Figure 5B), which is consistent with increased glucose catabolism, as glucose uptake and glucose transporter (GLUT1) expression were not affected by Sirt2 deficiency (Figure 5D). Concomitantly, Sirt2<sup>-/-</sup> T cells displayed increased levels of early glycolytic intermediates and serine. Serine is neo-synthesized from the glycolytic intermediate 3-phosphoglycerate to support nucleotide synthesis in proliferating T cells (Ma et al., 2017). Sirt2<sup>-/-</sup> T cells also displayed increased levels of extracellular lactate, confirming increased

aerobic glycolysis. Despite an increase in pyruvate conversion to lactate, Sirt2<sup>-/-</sup> T cells exhibited increased levels of late TCA-cycle intermediates, consistent with increased glutaminolysis and FAO fueling the TCA-cycle (Figures 5A–5C).

We further conducted a targeted LC-MS/MS analysis of FAO intermediates in activated WT versus Sirt2<sup>-/-</sup> CD8<sup>+</sup> T cells. Strikingly, Sirt2<sup>-/-</sup> T cells displayed higher levels of acyl-carnitines (C14-C4) with increased acetyl-CoA, the end product of FAO, consistent with enhanced FA catabolism (Figure 5E).

An increase in total acyl-carnitine levels (Figure 5E, pie chart) and mitochondrial resistance to etomoxir in Sirt2<sup>-/-</sup> T cells suggested altered regulation of CPT1 $\alpha$ . Indeed, both mRNA and protein levels of CPT1 $\alpha$  were upregulated in Sirt2<sup>-/-</sup> T cells (Figures 5F and 5G), which may complement enhanced TFP activity in supporting enhanced FAO.

Consistent with a hyper-metabolic phenotype, Sirt2<sup>-/-</sup> T cells displayed higher ATP/ADP ratio (Figure 5H), and together, these results indicate that Sirt2 is a master regulator of key metabolic pathways in activated T cells.

### Dynamic Evolution of Sirt2 Interactome during T Cell Activation and Maturation

To understand Sirt2 regulation of metabolic pathways in the physiologic context of T cell activation and maturation, Sirt2 interactions with the 12 metabolic targets described above were quantified within naive, activated, and T<sub>M</sub> cell subsets using IP-MS/MS analyses on CD3<sup>+</sup> T<sub>N</sub> cells versus activated T cells and CD4<sup>+</sup> OT-II T<sub>N</sub> cells versus T<sub>M</sub> cells (Figure 6).

Interestingly, Sirt2 interaction with a majority of the glycolytic targets was higher in activated T cells and T<sub>M</sub> cells compared with T<sub>N</sub> cells. Similarly, Sirt2 interaction with ASCT2 was increased in activated T cells but returned closer to naive levels in T<sub>M</sub> cells, where glutaminolysis was less involved. In contrast, Sirt2 interaction with TFP from the FAO pathway decreased upon activation and remained relatively low during the memory stage. The pattern of Sirt2 interaction with the TCA enzymes was complex, but Sirt2 uncoupling from ACO2 and SUCLG1 in T<sub>M</sub> cells was consistent with increased OxPhos in these cells (Figure 6). These findings demonstrate a dynamic change in Sirt2 substrate specificity during the T cell activation and maturation.

### Sirt2 Deficiency Delays Tumor Progression In Vivo

As Sirt2 deficiency endows T cells with superior metabolic fitness and effector functions *ex vivo*, we investigated the impact of Sirt2 deficiency on antitumor immune responses *in vivo*. Sirt2<sup>-/-</sup> recipient mice transplanted intravenously (i.v.) with

(D and E) Cytotoxic activities of WT versus Sirt2<sup>-/-</sup> CD8<sup>+</sup> Pmel T cells after co-culture with B16F10 cells with 2 mM 2-DG (D) or 100 nM Oligo (E) (n = 3).

(F) IFN- $\gamma$  ELISPOT assay on WT versus Sirt2<sup>-/-</sup> CD3<sup>+</sup> TILs after re-challenge with irradiated B16F10 cells at the indicated concentration of 2-DG (n = 3).

(G) The schematic shows UK5099, BPTES, and etomoxir targets.

(H) OCR of activated WT (upper panel) and Sirt2<sup>-/-</sup> (lower panel) CD3<sup>+</sup> T cells (n = 10–12). BPTES, Etomoxir, or UK5099 followed by Oligo, FCCP, and R/A were injected at the indicated time points.

(I) OCR of WT (upper panel) and Sirt2<sup>-/-</sup> (lower panel) TILs (n = 4–7). Vehicle or etomoxir followed by Oligo, FCCP, and R/A were injected at the indicated time points.

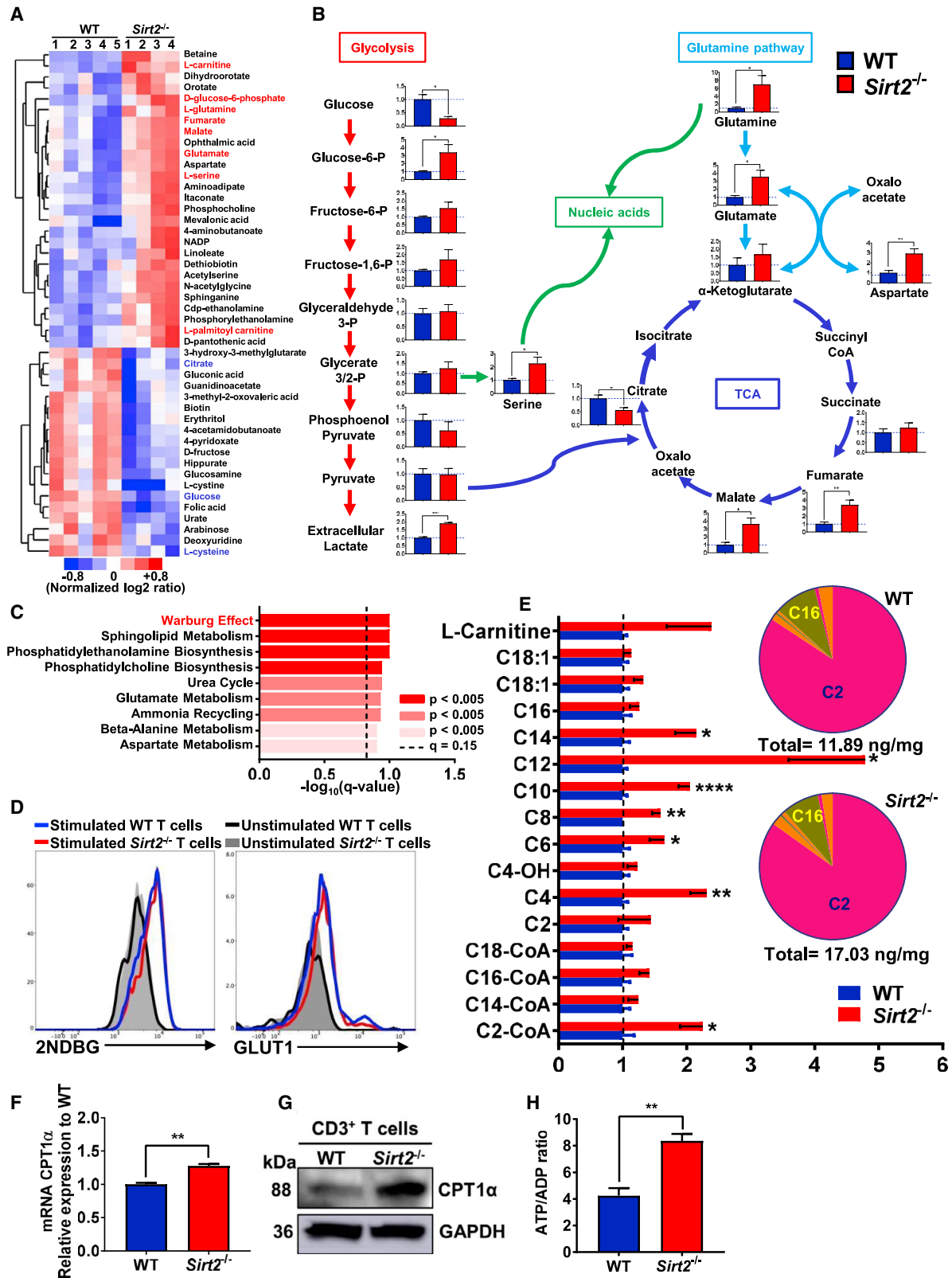
(J) Consumption of exogenous and endogenous FA by WT versus Sirt2<sup>-/-</sup> CD3<sup>+</sup> T cells (n = 4–6).

(K) Left, Schematic of T<sub>M</sub> cell generation steps *ex vivo*. Right, frequency of live CD4<sup>+</sup> OT-II (n = 4) and CD8<sup>+</sup> Pmel (n = 3) T<sub>M</sub> cells.

(L and M) Left, cell viability was determined by annexin V and DAPI staining on CD4<sup>+</sup> OT-II T<sub>M</sub> cells (L) and CD8<sup>+</sup> Pmel T<sub>M</sub> cells (M). Right, frequency of total apoptotic CD4<sup>+</sup> OT-II T<sub>M</sub> cells (n = 4) (L); and CD8<sup>+</sup> Pmel T<sub>M</sub> cells (n = 3) (M).

Data are mean  $\pm$  SEM. \*p < 0.05, \*\*p < 0.01, \*\*\*p < 0.001, \*\*\*\*p < 0.0001.

See also Figure S4.



(legend on next page)

B16F10 melanoma cells had a markedly reduced number of lung metastases compared with WT recipient mice (Figure 7A). There was also a significant delay in the growth of s.c.-transplanted B16F10 tumors and Lewis lung cancer (LLC) tumors in Sirt2<sup>-/-</sup> mice versus WT mice (Figures 7B and S6A). Notably, superior anti-PD-1 therapeutic responses were observed in Sirt2<sup>-/-</sup> recipient mice after i.v. challenge with B16F10 cells (Figure 7C).

Importantly, the depletion of either CD8<sup>+</sup> or CD4<sup>+</sup> T cells abrogated superior tumor control in Sirt2<sup>-/-</sup> mice, confirming that the protective effect of Sirt2 deficiency relied on both T cell subsets (Figure 7D). Furthermore, adoptive transfer of Sirt2<sup>-/-</sup> CD8<sup>+</sup> Pmel T cells into the immunodeficient NOD Scid gamma (NSG) mice, significantly reduced lung metastases after i.v. B16F10 challenge versus adoptive transfer of WT CD8<sup>+</sup> Pmel T cells (Figure 7E).

Phenotypic characterization of TILs isolated from s.c. B16F10 tumors revealed accumulation of CD8<sup>+</sup> effector memory T (T<sub>EM</sub>) cells and the terminally differentiated CD27<sup>-</sup>CD8<sup>+</sup> T cells, as well as an increase in the PD-1 expression with Sirt2 deficiency (Figures 7F, 7G, and S6B). Similar phenotypic changes were observed in the secondary lymphoid organs of Sirt2<sup>-/-</sup> mice upon i.v. tumor challenge, whereas no qualitative or quantitative phenotypic differences were observed between unchallenged WT and Sirt2<sup>-/-</sup> mice (Figures S6C–S6E). More importantly, Sirt2<sup>-/-</sup> TILs exhibited increased proliferation and IFN- $\gamma$  release with superior cytotoxic activity (Figures 7H–7J and S6F). Collectively, these phenotypic and functional changes in Sirt2<sup>-/-</sup> TILs cells are consistent with a hyper-reactive phenotype and superior antitumor activity.

We, therefore, investigated whether the superior tumor rejection in Sirt2<sup>-/-</sup> mice depended also on glycolysis and OxPhos. Sirt2<sup>-/-</sup> versus WT Pmel T cells were treated with 2-DG or Oligo, and then adoptively transferred into NSG mice i.v. challenged with B16F10 cells. Interestingly, both 2-DG and Oligo abrogated the superior antitumor effect of Sirt2<sup>-/-</sup> Pmel T cells (Figure 7K), confirming that the protective effect of Sirt2 deficiency relied on both glycolysis and OxPhos.

### Sirt2 Inhibition Augments the Antitumor Activity of Human T Cells

To determine the translational potential of the Sirt2 blockade on human samples, we investigated the effect of Sirt2 inhibition in human T cells using two Sirt2 inhibitors: AGK2 and Thiomyristoyl (TM). Consistent with our mouse studies, AGK2 and TM treat-

ment of human CD3<sup>+</sup> T cells from healthy donors increased aerobic glycolysis, OxPhos, and IFN- $\gamma$  production (Figures S7A–S7F). Increased acetylation level of  $\alpha$ -tubulin, a Sirt2 substrate, was observed with both AGK2 and TM treatments (Figures S7G and S7H). Further, human TILs isolated from NSCLC patient samples treated with AGK2 also exhibited increased aerobic glycolysis, OxPhos, and IFN- $\gamma$  production (Figures 7L–7N). More importantly, when patient TILs expanded *ex vivo* were co-cultured with their autologous tumor cells, AGK2 enhanced their cytotoxic activity (Figure 7O). Therefore, Sirt2 inhibition emerges as a promising intervention to enhance the metabolic fitness of tumor-reactive T cells in the context of cell therapy.

### DISCUSSION

Although cancer immunotherapies targeting immune checkpoints have redefined cancer treatment, several cancers remain resistant and new strategies are urgently needed (Gide et al., 2018; Li et al., 2018). Sirt2 has long been a topic of debate due to conflicting reports on its dual tumor-suppressor and oncogenic roles in cancer (Jing et al., 2016; McGlynn et al., 2014). Herein, we show that Sirt2 is an immune checkpoint with a broad involvement in regulating multiple metabolic pathways that are crucial to T cell functions, and therapeutic targeting of Sirt2 promotes metabolic fitness of T cells to improve antitumor immunity.

Mechanistically, Sirt2 impacts the acetylation status and the activity of key enzymes of glycolysis, TCA-cycle, FAO, and glutaminolysis. Although Sirt2 regulation of glycolysis has not been previously described in T cells, prior studies in induced pluripotent stem cells (Cha et al., 2017) and HeLa cells (Park et al., 2016) demonstrated Sirt2 interaction with the glycolytic enzymes. Importantly, Sirt2 interaction with the TCA-cycle, FAO, and glutaminolysis enzymes has not been previously reported.

As a consequence of their hyper-metabolic phenotype, Sirt2<sup>-/-</sup> T cells display increased proliferation, survival, and effector functions, and thus, efficiently reject transplantable tumors *in vivo*. Notably, there are increases in T<sub>EM</sub> cells in Sirt2<sup>-/-</sup> mice upon tumor challenge. T<sub>EM</sub> cells play an essential role in tumor-specific immune response (Mami-Chouaib et al., 2018), and their high frequency correlates with favorable prognosis in cancer patients (Pagès et al., 2005). In addition, PD-1 expression is increased in Sirt2<sup>-/-</sup> TILs and its blockade synergizes with the protective effect of Sirt2 deficiency against tumor challenge.

### Figure 5. Metabolic Reprogramming in Activated Sirt2<sup>-/-</sup> T Cells

(A) Heatmaps of differentially expressed metabolites in WT (n = 5) versus Sirt2<sup>-/-</sup> (n = 4) CD8<sup>+</sup> T cells.

(B) Relative levels of metabolites implicated in glycolysis, TCA-cycle, and glutaminolysis are shown. Samples are normalized to WT T cells, as indicated by dashed lines.

(C) Metabolite set enrichment analysis of the upregulated metabolic pathways in Sirt2<sup>-/-</sup> CD8<sup>+</sup> T cells compared with WT. A false discovery rate q value < 0.15 was used as a cut-off.

(D) 2-NBDG uptake (left panel) and GLUT1 expression (right panel) in WT versus Sirt2<sup>-/-</sup> CD8<sup>+</sup> T cells (n = 3).

(E) Relative levels of free carnitine, acyl-carnitines, acyl-CoA, and acetyl-CoA in WT (n = 5) versus Sirt2<sup>-/-</sup> (n = 6) CD8<sup>+</sup> T cells. Samples are normalized to WT T cells, as indicated by dashed lines. Pie charts indicate the relative abundance of different acyl-carnitines (C2–C18). Total numbers indicate the number of combined acyl-carnitines.

(F) Relative CPT1 $\alpha$  mRNA levels were determined by RNA-seq analysis on activated WT versus Sirt2<sup>-/-</sup> CD4<sup>+</sup> T cells. Samples are normalized to WT T cells (n = 3).

(G) WB of CPT1 $\alpha$  protein levels in activated WT versus Sirt2<sup>-/-</sup> CD3<sup>+</sup> T cells. GAPDH levels were used as loading control.

(H) ATP/ADP ratio in activated WT versus Sirt2<sup>-/-</sup> CD3<sup>+</sup> T cells (n = 3).

Data are mean  $\pm$  SEM. \*p < 0.05, \*\*p < 0.01.

See also Figure S5.

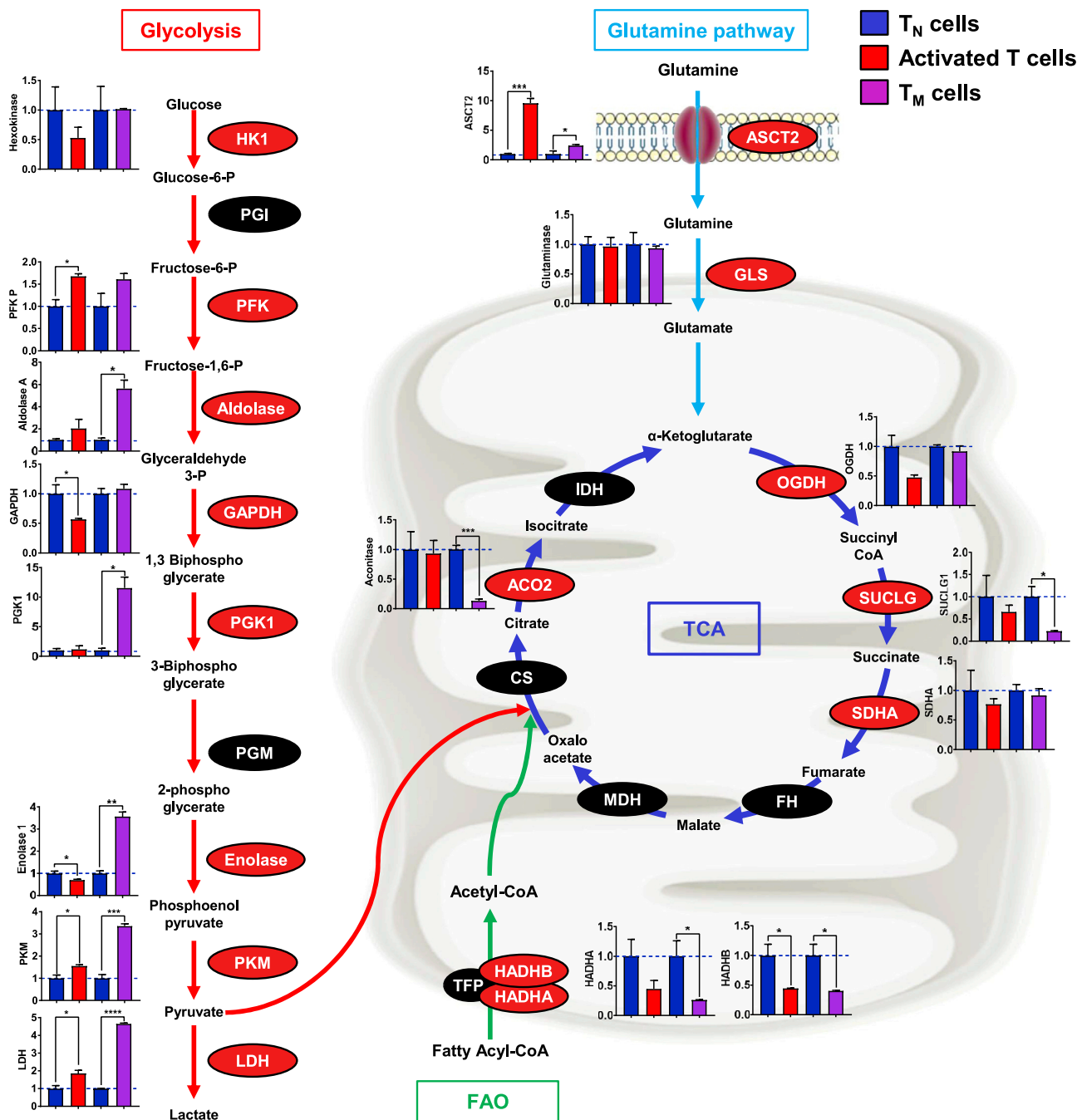


**Figure 6. Dynamic Evolution of Sirt2 Interactome during T cell Activation and Maturation**

Schematic diagram of glycolysis, TCA-cycle, FAO, and glutaminolysis. Enzymes identified to interact with Sirt2 via IP-MS/MS analysis are indicated in red. Relative interaction of Sirt2 with each target is shown in  $CD3^+ T_N$  cells versus activated T cells and  $CD4^+ OT-II T_N$  cells versus  $T_M$  cells. Samples are normalized to  $T_N$  cells (n = 3). Data are mean  $\pm$  SEM. \*p < 0.05, \*\*p < 0.01, \*\*\*p < 0.001, \*\*\*\*p < 0.0001.

PD-1 is paradoxically a marker of activated tumor-reactive  $CD8^+$  T cells in melanoma, and tumor regression with PD-1 blockade requires pre-existing PD-1<sup>+</sup>  $CD8^+$  T cells (Tumeh et al., 2014).

The immunologic functions of Sirtuins have been previously focused on Sirt1 and Sirt3. Notably, downregulation of Sirt1 expression in T cells led to their enhanced glycolytic and cytotoxic capacity (Jeng et al., 2018), while Sirt3 deficient T cells

manifested a hypo-reactive phenotype (Toubai et al., 2018). However, Sirt1 and Sirt3-7 levels remained unchanged between WT and Sirt2<sup>-/-</sup> T cells, suggesting that the immune and metabolic functions of Sirt2 are independent of other Sirtuins. Interestingly, Jeng et al. (2018) demonstrated that resveratrol, which promotes Sirt1 activity, decreased glycolytic activity of  $CD8^+ CD28^- Sirt1^{LOW}$  T cells. However, resveratrol is also an agonist

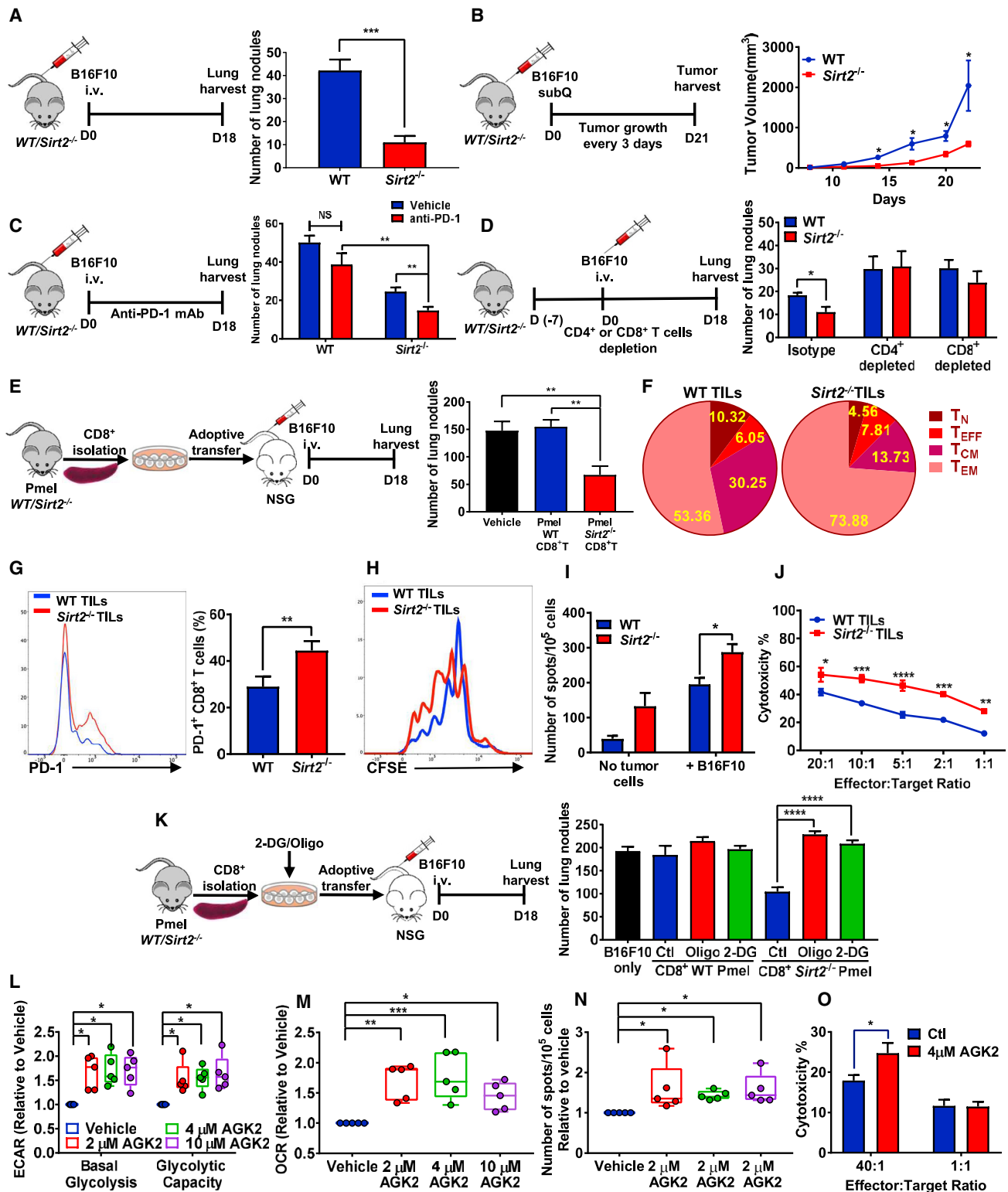


**Figure 7. Sirt2 Deficiency Augments Tumor Immunity in Mice and Humans**

(A) Number of lung metastatic nodules in WT versus *Sirt2*<sup>-/-</sup> mice i.v. challenged with B16F10 cells (n = 5).

(B) Subcutaneous B16F10 tumor growth curves of WT versus *Sirt2*<sup>-/-</sup> mice (n = 5).

(C) Number of lung metastatic nodules in WT versus *Sirt2*<sup>-/-</sup> mice i.v. challenged with B16F10 cells and treated with vehicle or anti-PD-1 (n = 6).

(legend continued on next page)

of Sirt2 activity (Pan et al., 2017), and decreased glycolysis by resveratrol may also be in part through Sirt2 activity.

Among the glycolytic targets modulated by Sirt2, GAPDH and ENO1 have been directly implicated in T cell functions. GAPDH is known to directly bind to IFN- $\gamma$  mRNA and block its translation (Chang et al., 2013). A recent study showed that the acetylated form of GAPDH exhibits superior enzymatic activity and low affinity for IFN- $\gamma$  mRNA (Balmer et al., 2016), in accordance with the effects observed in Sirt2<sup>-/-</sup> T cells. Moreover, a prior study demonstrated downregulation of ENO1 activity without changes in its mRNA or protein levels in human and murine melanoma TILs, leading to metabolically compromised TILs (Gemta et al., 2019). Although the precise mechanism was not identified, authors concluded that ENO1 activity is likely post-translationally regulated in TILs (Gemta et al., 2019). Because Sirt2 is upregulated in TILs and ENO1 is a Sirt2 substrate, we posit that the suppressed ENO1 activity in TILs observed by Gemta et al. may be attributable to Sirt2 deacetylase activity.

While Sirt2<sup>-/-</sup> T cells exhibit enhanced glycolysis and glutaminolysis, excess glucose and glutamine uptake by cancer cells often depletes the TME from these nutrients (Chang et al., 2015). In this context, TILs require alternate fuel sources to meet their metabolic demands. Indeed, CD8<sup>+</sup> TILs enhance FAO to preserve their functions within the hypoglycemic TME, and promoting FA catabolism improves CD8<sup>+</sup> TIL functions (Zhang et al., 2017). Interestingly, a majority of TILs are T<sub>M</sub> cells, which preferentially utilize FAO to persist and mediate a protective immunity (van der Windt et al., 2013). Therefore, improved survival of Sirt2<sup>-/-</sup> T<sub>M</sub> cells associated with enhanced FAO may contribute to superior antitumor immunity. Similar to T<sub>M</sub> cells, activated Sirt2<sup>-/-</sup> T cells exhibit superior reliance on endogenous FA (O'Sullivan et al., 2014). Although the mechanism of this unique phenotype is not well understood, utilization of endogenous FA by Sirt2<sup>-/-</sup> T cells may confer higher capacity for survival and immune response within the TME, where exogenous FA may not be readily available.

Our analysis on the evolution of Sirt2 interactome during T cell activation and maturation provides an insight into the physiologic role of Sirt2 throughout T cell ontogeny. In activated T cells, increased Sirt2 interaction with the glycolytic targets and ASCT2, combined with upregulation of total Sirt2 levels, highlight the role of Sirt2 as a brake on glycolysis and glutaminolysis to prevent uncontrolled proliferative responses. Notably, in T<sub>M</sub> cells, Sirt2 seems to predominantly interact with the glycolytic

pathway and uncouple from FAO enzymes to allow a metabolic switch toward FAO with a quiescent state. The pattern of Sirt2 interaction with the TCA-cycle is more complex, reflecting the convergence of multiple metabolic pathways from different fuel sources to this final step of OxPhos. Thus, we speculate that Sirt2 interactions change instantly depending on the active metabolic pathway influenced by nutrient availability. Such dynamic changes in Sirt2 expression levels and its substrate specificity corroborate the idea that Sirt2 functions as a metabolic checkpoint orchestrating multiple metabolic pathways to precisely direct the energetic state and fate of T cells by promoting a metabolically quiescent phenotype.

Several metabolic regulators, such as c-Myc, HIF-1 $\alpha$ , LKB1/STK11, GAPDH, ENO1, and PEP, were described as critical metabolic checkpoints in immune homeostasis and antitumor immunity (Chang et al., 2013; Doedens et al., 2013; Gemta et al., 2019; He et al., 2017; Wang et al., 2011). However, targeting these metabolic checkpoints has proven difficult due to hurdles in generating selective drugs or unintended toxicity. In this regard, the Sirt2 blockade using selective inhibitors offers a unique opportunity to manipulate T cell metabolism and augment cancer immunotherapy.

Notably, the Sirt2 blockade appears to synergize with the PD-1 blockade. Therefore, pharmacologic inhibition of Sirt2 in combination with PD-1 blockers may be an effective immunotherapy strategy. In addition, contrary to primary cells, Sirt2 inhibition has been shown to have an antitumor activity in cancer cells via c-Myc degradation (Jing et al., 2016), suggesting that pharmacologic intervention may suppress tumor while promoting antitumor immunity. Alternatively, manipulation of Sirt2 could be achieved by gene editing during TIL expansion or chimeric antigen receptor (CAR) T cell generation *ex vivo*, thus, selectively targeting T cells. The poor clinical response to TIL therapy observed in NSCLC patients with elevated Sirt2 levels in TILs underscores that the Sirt2 blockade may augment the potency and persistence of TILs or CAR T cells by improving their metabolic fitness.

In summary, we report that Sirt2 inhibition enhances tumor-specific T cell responses by promoting metabolic reprogramming toward a profound hyper-metabolic state with enhanced capacity for aerobic glycolysis and OxPhos in murine and human T cells, thus, revealing a striking role for Sirt2 as a prominent metabolic checkpoint. Importantly, Sirt2 is an actionable target via pharmacologic or genetic strategies, pointing to tractable

(D) Number of lung metastatic nodules in WT versus Sirt2<sup>-/-</sup> mice treated with isotype control, anti-CD4, or anti-CD8 antibodies before B16F10 i.v. challenge (n = 5).

(E) Number of lung metastatic nodules in NSG mice i.v. challenged with B16F10 cells and adoptively transferred with WT versus Sirt2<sup>-/-</sup> CD8<sup>+</sup> Pmel T cells (n = 8).

(F) Pie charts show mean percentages of T<sub>N</sub>, T<sub>EFF</sub>, T<sub>EM</sub>, and T<sub>CM</sub> (central memory) CD8<sup>+</sup> T cell subsets among WT versus Sirt2<sup>-/-</sup> TILs (n = 3–4).

(G) Left, PD-1 expression in WT versus Sirt2<sup>-/-</sup> TILs by flow cytometry. Right, frequency of PD1<sup>+</sup>CD8<sup>+</sup> TILs (n = 3–4).

(H) Proliferation of CFSE-labeled WT versus Sirt2<sup>-/-</sup> TILs (n = 4).

(I) IFN- $\gamma$  ELISPOT assay on WT versus Sirt2<sup>-/-</sup> CD3<sup>+</sup> TILs (n = 3).

(J) Cytotoxic activities of WT versus Sirt2<sup>-/-</sup> CD3<sup>+</sup> TILs after co-culture with B16F10 cells (n = 3).

(K) Number of lung metastatic nodules in NSG mice i.v. challenged with B16F10 cells and adoptively transferred with WT versus Sirt2<sup>-/-</sup> CD8<sup>+</sup> Pmel T cells pretreated with vehicle (Ctl), Oligo, or 2-DG (n = 5–8).

(L–N) Human TILs were treated with AGK2 versus vehicle for 48 h. Basal glycolytic rate, glycolytic capacity (L), OCR (M), and number of IFN- $\gamma$  spots (N) of five human TILs samples were normalized to vehicle and plotted as shown.

(O) Cytotoxic activities of human TILs after co-culture with their autologous tumor cells with vehicle (Ctl) or 4  $\mu$ M AGK2 (n = 3).

Data are mean  $\pm$  SEM. \*p < 0.05, \*\*p < 0.01, \*\*\*p < 0.001, \*\*\*\*p < 0.0001.

See also Figures S6 and S7.

means to improve a broad spectrum of cancer immunotherapies.

### Limitations of Study

Our study demonstrated the role of Sirt2 in T cell metabolism and effector functions. However, the precise role of Sirt2 in different T cell subsets with distinct metabolic programs (e.g., Treg cells, Th1, Th2, and Th17 cells) has not been studied. Likewise, the potential role of Sirt2 in innate immunity remains elusive. Mechanistically, our study confirms Sirt2 interaction with 12 metabolic targets via LC-MS/MS and colP-IB experiments. However, the functional relevance of altered acetylation of specific lysine residues in each target remains unknown. Clinically, the prognostic relevance of Sirt2 expression in NSCLC TILs is limited by the small cohort size, and further validation will be necessary for clinical application. Also, the effects of Sirt2 inhibition in human T cells were examined using selective Sirt2 inhibitors, AGK2 and TM, which have been extensively used in research but are yet to be tested in clinical trials. Until development of a clinically active Sirt2 inhibitor, genetic manipulation will be the viable strategy for clinical translation.

### STAR★METHODS

Detailed methods are provided in the online version of this paper and include the following:

- **KEY RESOURCES TABLE**
- **RESOURCE AVAILABILITY**
  - Lead Contact
  - Materials Availability
  - Data and Code Availability
- **EXPERIMENTAL MODEL AND SUBJECT DETAILS**
  - Mice
  - Mouse T Cell Culture
  - Memory Differentiation
  - Human PBMC
  - Human TILs
  - Cell Lines
- **METHOD DETAILS**
  - Melanoma Lung Metastasis Model
  - Subcutaneous Tumor Models
  - Isolation of Mouse TILs
  - Construction and Production of Lentivectors
  - Lentivector Transduction
  - *In Vivo* T Cell Depletion
  - Adoptive Transfer of Pmel T Cells
  - Flow Cytometry
  - CFSE Dilution Assay
  - Enzyme-Linked Immunospot (ELISPOT) Assay
  - Lactate Dehydrogenase (LDH) Release Assay
  - Extracellular Flux Analysis
  - Enzyme Activity Assay
  - Lactate, Glutamine, and Glutamate Measurement
  - ADP/ATP Ratio Assay
  - Immunoprecipitation
  - Western Blot Analysis
  - Transmission Electron Microscopy
  - RNA-Sequencing Analysis

- Liquid Chromatography-Tandem Mass Spectrometry (LC-MS/MS)
- Untargeted Metabolomic Analysis
- Acyl-Carnitines, Acyl-CoA and Acetyl-CoA Analysis by LC-MS/MS
- Enrichment Analysis
- **QUANTIFICATION AND STATISTICAL ANALYSIS**

### SUPPLEMENTAL INFORMATION

Supplemental Information can be found online at <https://doi.org/10.1016/j.cmet.2020.07.008>.

### ACKNOWLEDGMENTS

This work was supported in part by National Institutes of Health grant K08 CA194273, American Cancer Society grant IRG-17-173-22, National Cancer Institute grant P30-CA076292, Dr. Miriam and Sheldon G. Adelson Medical Research Foundation, and H. Lee Moffitt Cancer Center and Research Institute Foundation. The authors acknowledge L. Van Kaer and J.E. Cleveland for discussing and reading the manuscript, G. DeNicola for advice on the metabolomic analysis, and S. Pilon-Thomas and B. Perez for sharing valuable resources.

### AUTHOR CONTRIBUTIONS

I.H. designed and performed experiments, analyzed and interpreted the data, and wrote the manuscript; L.Z., N.K., and C.I. contributed to *in vivo* experiments; M.-H.W. performed flow cytometry experiments; B.F. performed proteomic analysis; M.L. performed the metabolomic analysis; J.M.K. contributed to proteomic and metabolomic analyses; A.E.B. contributed to enrichment analysis; S.J.Y. performed RNA sequencing experiment; J.Y. contributed to gene expression profiling; R.W.E. performed microscopic evaluation; B.C.C. and S.J.A. generated human TILs and conducted the lung cancer TIL trial; J.R.C.-G. and J.J.M. made intellectual contributions to the manuscript; and S.K. designed experiments, analyzed and interpreted the data, and provided an overall direction. All authors have reviewed and approved the manuscript.

### DECLARATION OF INTERESTS

The authors declare no competing interests.

Received: November 22, 2019

Revised: May 21, 2020

Accepted: July 15, 2020

Published: August 7, 2020

### REFERENCES

- Balmer, M.L., Ma, E.H., Bantug, G.R., Grählert, J., Pfister, S., Glatter, T., Jauch, A., Dimeloe, S., Slack, E., Dehio, P., et al. (2016). Memory CD8<sup>+</sup> T cells require increased concentrations of acetate induced by stress for optimal function. *Immunity* 44, 1312–1324.
- Cha, Y., Han, M.J., Cha, H.-J., Zoldan, J., Burkart, A., Jung, J.H., Jang, Y., Kim, C.H., Jeong, H.-C., Kim, B.-G., et al. (2017). Metabolic control of primed human pluripotent stem cell fate and function by the miR-200c-SIRT2 axis. *Nat. Cell Biol.* 19, 445–456.
- Chang, C.H., Curtis, J.D., Maggi, L.B., Jr., Faubert, B., Villarino, A.V., O'Sullivan, D., Huang, S.C., van der Windt, G.J., Blagih, J., Qiu, J., et al. (2013). Posttranscriptional control of T cell effector function by aerobic glycolysis. *Cell* 153, 1239–1251.
- Chang, C.H., Qiu, J., O'Sullivan, D., Buck, M.D., Noguchi, T., Curtis, J.D., Chen, Q., Gindin, M., Gubin, M.M., van der Windt, G.J., et al. (2015). Metabolic competition in the tumor microenvironment is a driver of cancer progression. *Cell* 162, 1229–1241.

- Cox, J., and Mann, M. (2008). MaxQuant enables high peptide identification rates, individualized p.p.b.-range mass accuracies and proteome-wide protein quantification. *Nat. Biotechnol.* 26, 1367–1372.
- Creelan, B., Teer, J., Toloza, E., Mullinax, J., Landin, A., Gray, J., Tanvetyanon, T., Taddeo, M., Noyes, D., Kelley, L., et al. (2018). OA05.03 safety and clinical activity of adoptive cell transfer using tumor infiltrating lymphocytes (TIL) combined with nivolumab in NSCLC. *J. Thorac. Oncol.* 13, S330–S331.
- Doedens, A.L., Phan, A.T., Stradner, M.H., Fujimoto, J.K., Nguyen, J.V., Yang, E., Johnson, R.S., and Goldrath, A.W. (2013). Hypoxia-inducible factors enhance the effector responses of CD8<sup>+</sup> T cells to persistent antigen. *Nat. Immunol.* 14, 1173–1182.
- Eng, J.K., McCormack, A.L., and Yates, J.R. (1994). An approach to correlate tandem mass spectral data of peptides with amino acid sequences in a protein database. *J. Am. Soc. Mass Spectrom.* 5, 976–989.
- Gemta, L.F., Siska, P.J., Nelson, M.E., Gao, X., Liu, X., Locasale, J.W., Yagita, H., Slingluff, C.L., Jr., Hoehn, K.L., Rathmell, J.C., and Bullock, T.N.J. (2019). Impaired enolase 1 glycolytic activity restrains effector functions of tumor-infiltrating CD8<sup>+</sup> T cells. *Sci. Immunol.* 4, eaap9520.
- Gide, T.N., Wilmott, J.S., Scolyer, R.A., and Long, G.V. (2018). Primary and acquired resistance to immune checkpoint inhibitors in metastatic melanoma. *Clin. Cancer Res.* 24, 1260–1270.
- Gomes, P., Fleming Outeiro, T., and Cavadas, C. (2015). Emerging role of sirtuin 2 in the regulation of mammalian metabolism. *Trends Pharmacol. Sci.* 36, 756–768.
- Guarente, L. (2011). Franklin H. Epstein lecture: sirtuins, aging, and medicine. *N. Engl. J. Med.* 364, 2235–2244.
- Haug, K., Cochrane, K., Nainala, V.C., Williams, M., Chang, J., Jayaseelan, K.V., and O'Donovan, C. (2020). MetaboLights: a resource evolving in response to the needs of its scientific community. *Nucleic Acids Res* 48, D440–D444.
- He, L., Gomes, A.P., Wang, X., Yoon, S.O., Lee, G., Nagiec, M.J., Cho, S., Chavez, A., Islam, T., Yu, Y., et al. (2018). mTORC1 promotes metabolic reprogramming by the suppression of GSK3-dependent Foxk1 phosphorylation. *Mol. Cell* 70, 949–960.e4.
- He, N., Fan, W., Henriquez, B., Yu, R.T., Atkins, A.R., Liddle, C., Zheng, Y., Downes, M., and Evans, R.M. (2017). Metabolic control of regulatory T cell (Treg) survival and function by Lkb1. *Proc. Natl. Acad. Sci. USA* 114, 12542–12547.
- Houtkooper, R.H., Pirinen, E., and Auwerx, J. (2012). Sirtuins as regulators of metabolism and healthspan. *Nat. Rev. Mol. Cell Biol.* 13, 225–238.
- Jeng, M.Y., Hull, P.A., Fei, M., Kwon, H.S., Tsou, C.L., Kasler, H., Ng, C.-P., Gordon, D.E., Johnson, J., Krogan, N., et al. (2018). Metabolic reprogramming of human CD8<sup>+</sup> memory T cells through loss of SIRT1. *J. Exp. Med.* 215, 51–62.
- Jing, H., Hu, J., He, B., Negrón-Abril, Y.L., Stupinski, J., Weiser, K., Carbonaro, M., Chiang, Y.L., Southard, T., Giannakakou, P., et al. (2016). A SIRT2-selective inhibitor promotes c-Myc oncoprotein degradation and exhibits broad anticancer activity. *Cancer Cell* 29, 297–310.
- Johnson, M.O., Wolf, M.M., Madden, M.Z., Andrejeva, G., Sugiura, A., Contreras, D.C., Maseda, D., Liberti, M.V., Paz, K., Kishton, R.J., et al. (2018). Distinct regulation of Th17 and Th1 cell differentiation by glutamine-dependent metabolism. *Cell* 175, 1780–1795.e19.
- Karmaus, P.W.F., Chen, X., Lim, S.A., Herrada, A.A., Nguyen, T.M., Xu, B., Dhungana, Y., Rankin, S., Chen, W., Rosencrance, C., et al. (2019). Metabolic heterogeneity underlies reciprocal fates of TH17 cell stemness and plasticity. *Nature* 565, 101–105.
- Li, X., Shao, C., Shi, Y., and Han, W. (2018). Lessons learned from the blockade of immune checkpoints in cancer immunotherapy. *J. Hematol. Oncol.* 11, 31.
- Liberzon, A., Birger, C., Thorvaldsdóttir, H., Ghandi, M., Mesirov, J.P., and Tamayo, P. (2015). The molecular signatures database (MSigDB) hallmark gene set collection. *Cell Syst* 1, 417–425.
- Lo Sasso, G., Menzies, K.J., Mottis, A., Piersigilli, A., Perino, A., Yamamoto, H., Schoonjans, K., and Auwerx, J. (2014). SIRT2 deficiency modulates macrophage polarization and susceptibility to experimental colitis. *PLoS One* 9, e103573.
- Lunt, S.Y., and Vander Heiden, M.G. (2011). Aerobic glycolysis: meeting the metabolic requirements of cell proliferation. *Annu. Rev. Cell Dev. Biol.* 27, 441–464.
- Ma, E.H., Bantug, G., Griss, T., Condotta, S., Johnson, R.M., Samborska, B., Mainolfi, N., Surí, V., Guak, H., Balmer, M.L., et al. (2017). Serine is an essential metabolite for effector T cell expansion. *Cell Metab* 25, 345–357.
- Mami-Chouaib, F., Blanc, C., Corgnac, S., Hans, S., Malenica, I., Granier, C., Tihy, I., and Tartour, E. (2018). Resident memory T cells, critical components in tumor immunology. *J. Immunother. Cancer* 6, 87.
- McGlynn, L.M., Zino, S., MacDonald, A.I., Curle, J., Reilly, J.E., Mohammed, Z.M., McMillan, D.C., Mallon, E., Payne, A.P., Edwards, J., and Shiels, P.G. (2014). SIRT2: tumour suppressor or tumour promoter in operable breast cancer? *Eur. J. Cancer* 50, 290–301.
- North, B.J., Marshall, B.L., Borra, M.T., Denu, J.M., and Verdin, E. (2003). The human Sir2 ortholog, SIRT2, is an NAD<sup>+</sup>-dependent tubulin deacetylase. *Mol. Cell* 11, 437–444.
- O'Sullivan, D., van der Windt, G.J., Huang, S.C., Curtis, J.D., Chang, C.H., Buck, M.D., Qiu, J., Smith, A.M., Lam, W.Y., DiPlato, L.M., et al. (2014). Memory CD8<sup>+</sup> T cells use cell-intrinsic lipolysis to support the metabolic programming necessary for development. *Immunity* 41, 75–88.
- Pagès, F., Berger, A., Camus, M., Sanchez-Cabo, F., Costes, A., Molidor, R., Mlecnik, B., Kirilovsky, A., Nilsson, M., Damotte, D., et al. (2005). Effector memory T cells, early metastasis, and survival in colorectal cancer. *N. Engl. J. Med.* 353, 2654–2666.
- Pan, Y., Zhang, H., Zheng, Y., Zhou, J., Yuan, J., Yu, Y., and Wang, J. (2017). Resveratrol exerts antioxidant effects by activating SIRT2 to deacetylate Prx1. *Biochemistry* 56, 6325–6328.
- Pardoll, D.M. (2012). The blockade of immune checkpoints in cancer immunotherapy. *Nat. Rev. Cancer* 12, 252–264.
- Park, S.H., Ozden, O., Liu, G., Song, H.Y., Zhu, Y., Yan, Y., Zou, X., Kang, H.J., Jiang, H., Principe, D.R., et al. (2016). SIRT2-mediated deacetylation and tetramerization of pyruvate kinase directs glycolysis and tumor growth. *Cancer Res.* 76, 3802–3812.
- Pearce, E.L., Poffenberger, M.C., Chang, C.H., and Jones, R.G. (2013). Fueling immunity: insights into metabolism and lymphocyte function. *Science* 342, 1242454.
- Perkins, D.N., Pappin, D.J., Creasy, D.M., and Cottrell, J.S. (1999). Probability-based protein identification by searching sequence databases using mass spectrometry data. *Electrophoresis* 20, 3551–3567.
- Rosenberg, S.A., and Restifo, N.P. (2015). Adoptive cell transfer as personalized immunotherapy for human cancer. *Science* 348, 62–68.
- Rothgiesser, K.M., Erener, S., Waibel, S., Lüscher, B., and Hottiger, M.O. (2010). SIRT2 regulates NF- $\kappa$ B-dependent gene expression through deacetylation of p65 Lys310. *J. Cell Sci.* 123, 4251–4258.
- Subramanian, A., Tamayo, P., Mootha, V.K., Mukherjee, S., Ebert, B.L., Gillette, M.A., Paulovich, A., Pomeroy, S.L., Golub, T.R., Lander, E.S., and Mesirov, J.P. (2005). Gene set enrichment analysis: a knowledge-based approach for interpreting genome-wide expression profiles. *Proc. Natl. Acad. Sci. USA* 102, 15545–15550.
- Toubai, T., Tamaki, H., Peltier, D.C., Rossi, C., Oravecz-Wilson, K., Liu, C., Zajac, C., Wu, J., Sun, Y., Fujiwara, H., et al. (2018). Mitochondrial deacetylase SIRT3 plays an important role in donor T cell responses after experimental allogeneic hematopoietic transplantation. *J. Immunol.* 201, 3443–3455.
- Tumeh, P.C., Harview, C.L., Yearley, J.H., Shintaku, I.P., Taylor, E.J., Robert, L., Chmielowski, B., Spasic, M., Henry, G., Ciobanu, V., et al. (2014). PD-1 blockade induces responses by inhibiting adaptive immune resistance. *Nature* 515, 568–571.
- van der Windt, G.J., O'Sullivan, D., Everts, B., Huang, S.C., Buck, M.D., Curtis, J.D., Chang, C.H., Smith, A.M., Ai, T., Faubert, B., et al. (2013). CD8 memory

T cells have a bioenergetic advantage that underlies their rapid recall ability. *Proc. Natl. Acad. Sci. USA* *110*, 14336–14341.

Verdin, E., Hirschey, M.D., Finley, L.W., and Haigis, M.C. (2010). Sirtuin regulation of mitochondria: energy production, apoptosis, and signaling. *Trends Biochem. Sci.* *35*, 669–675.

Vizcaíno, J.A., Deutsch, E.W., Wang, R., Csordas, A., Reisinger, F., Ríos, D., Dianes, J.A., Sun, Z., Farrah, T., Bandeira, N., et al. (2014). ProteomeXchange provides globally coordinated proteomics data submission and dissemination. *Nat. Biotechnol.* *32*, 223–226.

Wang, R., Dillon, C.P., Shi, L.Z., Milasta, S., Carter, R., Finkelstein, D., McCormick, L.L., Fitzgerald, P., Chi, H., Munger, J., and Green, D.R. (2011). The transcription factor Myc controls metabolic reprogramming upon T lymphocyte activation. *Immunity* *35*, 871–882.

Xia, J., and Wishart, D.S. (2010). MSEA: a web-based tool to identify biologically meaningful patterns in quantitative metabolomic data. *Nucleic Acids Res.* *38*, W71–W77.

Zhang, Y., Kurupati, R., Liu, L., Zhou, X.Y., Zhang, G., Hudaihed, A., Filisio, F., Giles-Davis, W., Xu, X., Karakousis, G.C., et al. (2017). Enhancing CD8<sup>+</sup> T cell fatty acid catabolism within a metabolically challenging tumor microenvironment increases the efficacy of melanoma immunotherapy. *Cancer Cell* *32*, 377–391.e9.

Zhao, E., Maj, T., Kryczek, I., Li, W., Wu, K., Zhao, L., Wei, S., Crespo, J., Wan, S., Vatan, L., et al. (2016). Cancer mediates effector T cell dysfunction by targeting microRNAs and EZH2 via glycolysis restriction. *Nat. Immunol.* *17*, 95–103.

Zhao, S., Xu, W., Jiang, W., Yu, W., Lin, Y., Zhang, T., Yao, J., Zhou, L., Zeng, Y., Li, H., et al. (2010). Regulation of cellular metabolism by protein lysine acetylation. *Science* *327*, 1000–1004.

STAR★METHODS

KEY RESOURCES TABLE

REAGENT or RESOURCE	SOURCE	IDENTIFIER
<b>Antibodies</b>		
Mouse monoclonal Anti-CPT1A antibody	Abcam	Cat#ab128568, Clone: 8F6AE9; RRID: AB_11141632
Goat polyclonal Anti-Rabbit IgG-HRP H&L antibody	Abcam	Cat#ab97051; RRID: AB_10679369
Rabbit monoclonal Anti-GAPDH antibody	Abcam	Cat#ab181602, Clone: EPR16891; RRID: AB_2630358
Rabbit monoclonal Anti-Hexokinase 1 antibody	Abcam	Cat#ab150423, Clone:EPR10134; RRID: N/A
Rabbit monoclonal Anti-LDH antibody	Abcam	Cat#ab52488, Clone: EP1566Y; RRID: AB_2134961
Rabbit monoclonal Anti-PFKP antibody	Abcam	Cat#ab204131, Clone: EPR17314; RRID: N/A
Rabbit monoclonal Anti-GLS antibody	Abcam	Cat#ab202027, Clone: EPR19525; RRID: N/A
Rabbit monoclonal Anti-GLUT1 antibody (Alexa Fluor 647)	Abcam	Cat#ab195020, Clone: EPR3915; RRID: AB_2783877
Rabbit monoclonal Anti-HADHA antibody	Abcam	Cat#ab203114, Clone: EPR17940; RRID: N/A
Rabbit polyclonal Anti-beta Actin antibody	Abcam	Cat#ab8227; RRID: AB_2305186
Rabbit polyclonal Anti-HIF-1 $\alpha$ antibody	Abcam	Cat#ab82832; RRID: AB_1860665
Rabbit polyclonal Anti-Sirt2 antibody	Abcam	Cat# ab67299; RRID: AB_1142864
Rabbit polyclonal Anti-HADHB antibody	Abcam	Cat#ab240601; RRID: N/A
Mouse monoclonal Anti-Rabbit IgG-HRP antibody (Light-Chain Specific)	Cell Signaling Technology	Cat#93702, Clone: D4W3E; RRID: AB_2800208
Rabbit mAb IgG XP® Isotype Control antibody	Cell Signaling Technology	Cat#3900, Clone: DA1E; RRID: AB_1550038
Rabbit monoclonal Anti-ACO2 antibody	Cell Signaling Technology	Cat#6571, Clone: D6D9; RRID: AB_2797630
Rabbit monoclonal Anti-Acetyl-tubulin antibody	Cell Signaling Technology	Cat#5335, Clone:D20G3; RRID: AB_10544694
Rabbit monoclonal Anti-Aldolase A antibody	Cell Signaling Technology	Cat#8060, Clone: D73H4; RRID: AB_2797635
Rabbit monoclonal Anti-PKM1/2 antibody	Cell Signaling Technology	Cat#3106, Clone: C5E6; RRID: AB_2283781
Rabbit monoclonal Anti-P-S6 antibody	Cell Signaling Technology	Cat#4858, Clone: D57.2.2E; RRID: AB_916156
Rabbit monoclonal Anti-ASCT2 antibody	Cell Signaling Technology	Cat#5345, Clone: V501; RRID: AB_10621427
Rabbit monoclonal Anti-SDHA antibody	Cell Signaling Technology	Cat#11998, Clone: D6J9M; RRID: AB_2750900
Rabbit monoclonal Anti-SUCLG1 antibody	Cell Signaling Technology	Cat#8071, Clone: D8A11; RRID: AB_10889930
Rabbit polyclonal Anti-Acetyl-lysine antibody	Cell Signaling Technology	Cat#9441; RRID: AB_331805
Rabbit polyclonal Anti-Enolase 1 antibody	Cell Signaling Technology	Cat#3810; RRID: AB_2246524
Rabbit polyclonal Anti- $\alpha$ -tubulin antibody	Cell Signaling Technology	Cat#2144; RRID: AB_2210548
Rabbit polyclonal Anti-c-Myc Antibody	Cell Signaling Technology	Cat#9402; RRID: AB_2151827

(Continued on next page)

**Continued**

REAGENT or RESOURCE	SOURCE	IDENTIFIER
Rabbit polyclonal Anti-Hexokinase1 antibody	Novus biologicals	Cat#NBP2-67503, Clone: ST47-05; RRID: N/A
Rabbit polyclonal Anti-PGK1 antibody	Novus biologicals	Cat#NBP2-67534; Clone:ST49-07; RRID: N/A
Rabbit polyclonal Anti-Sirt2 antibody	Sigma-Aldrich	Cat#S8447; RRID: AB_1079981
Hamster Anti-Mouse CD3 antibody (BUV395)	BD Biosciences	Cat#563565, Clone: 145-2C11; RRID: AB_2738278
Hamster Anti-Mouse PD-1 antibody (BV605)	BD Biosciences	Cat#563059, Clone: J43; RRID: AB_2737980
Mouse Anti-Human CD3 antibody (BUV496)	BD Biosciences	Cat#564809, Clone: UCHT1; RRID: AB_2744388
Mouse Anti-Human CD4 antibody (BUV737)	BD Biosciences	Cat#564305, Clone: SK3; RRID: AB_2713927
Mouse Anti-Human CD45RA antibody (FITC)	BD Biosciences	Cat#555488, Clone: HI100; RRID: AB_395879
Mouse Anti-Human CD8 antibody (BUV395)	BD Biosciences	Cat#563795, Clone: RPA-T8; RRID: AB_2722501
Mouse Anti-Mouse NK 1.1 antibody (PE)	BD Biosciences	Cat#553165, Clone: PK136; RRID: AB_394677
Rat Anti-Mouse B220 antibody (APC-H7)	BD Biosciences	Cat#565371, Clone: RA3-6B2; RRID: AB_2739208
Rat Anti-Mouse CD19 antibody (PerCP-Cy <sup>5</sup> 5.5)	BD Biosciences	Cat#551001, Clone: 1D3; RRID: AB_394004
Rat Anti-Mouse CD4 antibody (BUV805)	BD Biosciences	Cat#612900 Clone: GK1.5; RRID: AB_2827960
Rat Anti-Mouse F4/80 antibody (BV711)	BD Biosciences	Cat#565612, Clone: T45-2342; RRID: AB_2734769
Rat Anti-Mouse Gr-1 antibody (BUV395)	BD Biosciences	Cat#563849, Clone: RB6-8C5; RRID: AB_2738450
Rat Anti-Mouse IFN- $\gamma$ antibody (BV711)	BD Biosciences	Cat#564336, Clone: XMG1.2; RRID:AB_2738752
Hamster Anti-Mouse CD11c antibody (Alexa Fluor 488)	Biologend	Cat#117311, Clone: N418; RRID: AB_389306
Hamster Anti-Mouse CD27 antibody (BV510)	Biologend	Cat#124229, Clone: LG.3A10; RRID: AB_2565795
Mouse Anti-Mouse Granzyme B antibody (Alexa647)	Biologend	Cat#515406, Clone: GB11; RRID:AB_2566333
Rat Anti-Mouse CD11b antibody (BV605)	Biologend	Cat#101257, Clone: M1/70; RRID: AB_2565431
Rat Anti-Mouse CD44 antibody (Alexa Fluor 488)	Biologend	Cat#103016, Clone: IM7; RRID: AB_493679
Rat Anti-Mouse CD62L antibody (PE-Cy7)	Biologend	Cat#104418, Clone: MEL-14; RRID: AB_313103
Rat Anti-Mouse CD8 antibody (Alexa Fluor 700)	Biologend	Cat#100730 Clone: 53-6.7; RRID: AB_493703
Rat Anti-Mouse I-A/I-E antibody (Alexa Fluor 647)	Biologend	Cat#107618, Clone: M5/114.15.2; RRID: AB_493525
Rat Anti-Mouse KI-67 antibody (APC)	Biologend	Cat# 652406, Clone: 16A8; RRID: AB_2561930
Rat Anti-Mouse TNF- $\alpha$ antibody (FITC)	Biologend	Cat#506304, Clone: MP6-XT22; RRID: AB_315425
PBS57-loaded CD1d tetramer (Alexa647)	NIH Tetramer Facility	N/A
Goat Anti-Rabbit IgG antibody (Alexa647)	Thermo Fisher Scientific	Cat#A32733; RRID: AB_2633282

(Continued on next page)

**Continued**

REAGENT or RESOURCE	SOURCE	IDENTIFIER
Monoclonal Anti-Human CD3 antibody	BioXCell	Cat#BE0001-2, Clone: OKT-3; RRID: AB_1107632
Monoclonal Anti-Mouse CD3 antibody	BioXCell	Cat# BE0001-1, Clone: 145-2C11; RRID: AB_1107634
Monoclonal Anti-Mouse PD-1 antibody	BioXCell	Cat#BE0146, Clone: RMP1-14; RRID: AB_10949053
Monoclonal Anti-Mouse CD4 antibody	BioXCell	Cat#BE0003-1, Clone: GK1.5; RRID: AB_1107636
Monoclonal Anti-Mouse CD8 antibody	BioXCell	Cat#BE0061, Clone: 2.43; RRID: AB_1125541
Rat IgG2b Isotype Control antibody	BioXCell	Cat#BE0090, Clone: LTF-2; RRID: AB_1107780
Monoclonal Anti-Human IFN- $\gamma$ antibody	Mabtech, Inc.	Cat#3420-3-250, Clone: 1-D1K; RRID: AB_907283
Biotinylated anti-IFN- $\gamma$ antibody	Mabtech, Inc.	Cat#3321-6-250, Clone: R4-6A2; RRID: AB_2280104
Monoclonal Rat Anti-Mouse IFN- $\gamma$ antibody	Mabtech, Inc.	Cat#3321-3-250, Clone AN-18; RRID: AB_907279
<b>Biological Samples</b>		
Healthy adult peripheral blood	OneBlood	N/A
Human tumor infiltrating lymphocytes	Dr. B Creelan and Dr. S Antonia, H. Lee Moffitt Cancer Center Tampa, FL, USA	N/A
<b>Chemicals, Peptides, and Recombinant Proteins</b>		
Seahorse XF 1.0 M glucose solution	Agilent technologies	Cat#103577-100
Seahorse XF 100 mM pyruvate solution	Agilent technologies	Cat#103578-100
Seahorse XF 200 mM glutamine solution	Agilent technologies	Cat#103579-100
Seahorse XFe96FluxPak	Agilent technologies	Cat#102416-100
XF RPMI Medium pH 7.4	Agilent technologies	Cat#103576-100
gp100 (25 - 33), human	AnaSpec	Cat#AS-62589
DAPI	BD Biosciences	Cat#564907
Streptavidin-HRP	BD Biosciences	Cat#557630
AEC Substrate Kit	BD Biosciences	Cat#551951
BD Pharmingen™ Transcription Factor Buffer Set	BD Biosciences	Cat#562574
Cytofix/Cytoperm™ Buffer	BD Biosciences	Cat#554722
GolgiPlug™	BD Biosciences	Cat#555029
RBC Lysis Buffer	Biolegend	Cat#420301
Zombie Violet™ Fixable Viability Kit	Biolegend	Cat#423114
Immun-Blot PVDF membrane,	Bio-Rad	Cat#1704156
Fetal Bovine Serum	Biowest	Cat#S1520-500
Corning® Cell-Tak™ Cell and Tissue Adhesive	Corning	Cat#354240
Annexin V Apoptosis Detection Kit APC	eBioscience	Cat#17-8007-74
Ficoll-Paque™ PLUS Media	GE Healthcare	Cat#17144002
Percoll	GE Healthcare	Cat#17-0891-01
MitoTracker™ Green FM	Invitrogen	Cat#M7514
OVA 323-339	InvivoGen	Cat#VACISQ
Recombinant human rhIL-2	Peprtech	Cat#200-02
Recombinant Mouse IL-15 Protein	R&D Systems	Cat#447-ML-010
cOMplete™ Protease Inhibitor Cocktail	Roche Applied Science	Cat#11697498001
PhosSTOP Phosphatase Inhibitor	Roche Applied Science	Cat#4906845001

(Continued on next page)

**Continued**

REAGENT or RESOURCE	SOURCE	IDENTIFIER
TrueBlot® Anti-Rabbit Ig IP Agarose Bead Properties	Rockland	Cat#00-800-25
AGK2	Selleck Chemicals	Cat#S7577; CAS#304896-28-4
Thiomristoyl	Selleck Chemicals	Cat#S8245; CAS#1429749-41-6
2-Deoxy-D-glucose	Sigma-Aldrich	Cat#D6134; CAS# 154-17-6
Etomoxir	Sigma-Aldrich	Cat#E1905; CAS# 828934-41
Hepes	Sigma-Aldrich	Cat#H0887; CAS# 7365-45-9
Ionomycin	Sigma-Aldrich	Cat#10634; CAS#56092-82-1
L-Carnitine	Sigma-Aldrich	Cat#11242008001
Oligomycin	Sigma-Aldrich	Cat#O4876-5MG; CAS#1404-19-9
Phorbol 12-myristate 13-acetate	Sigma-Aldrich	Cat#P-8139; CAS#16561-29-8
Polybrene	Sigma-Aldrich	Cat#TR-1003
Lenti-X™ Concentrator	Takara Bio	Cat# 631232
2-NBDG	Thermo Fisher Scientific	Cat#N13195
Corning™ Hank's Balanced Salt Solutions (HBSS)	Thermo Fisher Scientific	Cat#MT21021CV
DMEM/F12	Thermo Fisher Scientific	Cat#11320033
Gentamicin	Thermo Fisher Scientific	Cat#15750-060
Pierce RIPA buffer,	Thermo Fisher Scientific	Cat#89900
Pierce™ ECL Western Blotting Substrate	Thermo Fisher Scientific	Cat#32106
RPMI 1640 medium	Thermo Fisher Scientific	Cat#11875-093
Super Signal West Femto Maximum Sensitivity Substrate kits	Thermo Fisher Scientific	Cat#34095
β-mercaptoethanol	Thermo Fisher Scientific	Cat#21985-023
Penicillin/Streptomycin	Thomas Scientific	Cat#C838W20
Human AB serum	Valley Biomedical, Inc.	Cat#HP1022
Collagenase Type IV	Worthington Biochemical	Cat#LS004186
DNase I	Sigma-Aldrich	Cat# 10104159001
<b>Critical Commercial Assays</b>		
Mito Fuel Flex Test Kit	Agilent technologies	Cat#103260-100
Palmitate-BSA FAO Substrate Kit	Agilent technologies	Cat#102720-100
Seahorse XF Cell Mito Stress Test Kit	Agilent technologies	Cat#103015-100
Seahorse XF Glycolysis Stress Test Kit	Agilent technologies	Cat#103020-100
Seahorse XF Glycolytic Rate Assay Kit	Agilent technologies	Cat#103344-100
Aconitase Activity Colorimetric Assay Kit	Biovision	Cat#K716
Aldolase Activity Colorimetric Assay Kit	Biovision	Cat#K665
Alpha-Ketoglutarate Dehydrogenase Activity Colorimetric Assay Kit	Biovision	Cat#K678
Enolase Activity Colorimetric/Fluorometric Assay Kit	Biovision	Cat#K691
GAPDH Activity Assay Kit	Biovision	Cat#K680
Hexokinase Colorimetric Assay Kit	Biovision	Cat#K789
Phosphofructokinase (PFK) Activity Colorimetric Assay Kit	Biovision	Cat#K776
Succinate Dehydrogenase Activity Colorimetric Assay Kit	Biovision	Cat#K660
Succinyl-CoA Synthetase Activity Colorimetric Assay Kit	Biovision	Cat#K597
Human Pan T cell isolation kit™	Miltenyi Biotec	Cat#130-096-535
Mouse CD3ε MicroBeads kit™	Miltenyi Biotec	Cat#130-094-973

(Continued on next page)

**Continued**

REAGENT or RESOURCE	SOURCE	IDENTIFIER
Mouse CD4+ T cell isolation kits™	Miltenyi Biotec	Cat#130-104-454
Mouse CD8+ T cell isolation kits™	Miltenyi Biotec	Cat#130-104-075
Mouse Pan T cell isolation kit™	Miltenyi Biotec	Cat#130-095-130
ADP/ATP Ratio Assay Kit	Sigma-Aldrich	Cat#MAK135
CellTrace™ CFSE Cell Proliferation Kit	Thermo Fisher Scientific	Cat#C34554
Pierce™ BCA Protein Assay Kit	Thermo Fisher Scientific	Cat#23225
Pierce™ LDH Cytotoxicity Assay Kit Catalog number	Thermo Fisher Scientific	Cat#88954
<b>Deposited Data</b>		
Mass spectrometry proteomic data for global Sirt2 interacting proteins	This paper. Dataset deposited to the ProteomeXchange Consortium via the PRIDE	PXD012811
Mass spectrometry proteomic data for the quantification of lysine acetylation	This paper. Dataset deposited to the ProteomeXchange Consortium via the PRIDE	PXD012796
Mass spectrometry proteomic data for the quantification of the metabolic Sirt2-interacting proteins in T <sub>N</sub> cells, activated T cells and T <sub>M</sub> cells	This paper. Dataset deposited to the ProteomeXchange Consortium via the PRIDE	PXD020150
Untargeted metabolomic LC-MS/MS analysis	This paper. Dataset deposited in MetaboLights database	MTBLS1795
Acyl-carnitines, acyl-CoA and acetyl-CoA LC-MS/MS analysis	This paper. Dataset deposited in MetaboLights database	MTBLS1832
The RNA-sequencing data	This paper. Dataset deposited in Gene Expression Omnibus	GSE151421
<b>Experimental Models: Cell Lines</b>		
B16-F10	ATCC	ATCC® CRL6475™; RRID: CVCL_0159
LLC	ATCC	ATCC® CRL-1642™; RRID: CVCL_4358
293T	ATCC	ATCC® CRL-3216™; RRID: CVCL_0063
<b>Experimental Models: Organisms/Strains</b>		
C57BL/6J mice	The Jackson Laboratory	Stock No: 000664
Pmel mice: B6.Cg- <i>Thy1<sup>a</sup></i> /Cy Tg(TcraTcrb)8Rest/J	The Jackson Laboratory	Stock No: 005023
Sirt2 <sup>-/-</sup> mice: B6.129-Sirt2 <sup>tm1.1Fwa</sup> /J	The Jackson Laboratory	Stock No: 012772
OT-II mice: B6.Cg-Tg(TcraTcrb)425Cbn/J	The Jackson Laboratory	Stock No: 004194
NOD scid gamma (NSG) mice: NOD.Cg- <i>Prkdc<sup>scid</sup> Il2rg<sup>tm1Wjl</sup>/SzJ</i>	The Jackson Laboratory	Stock No: 005557
Sirt2 <sup>-/-</sup> Pmel mice	This paper	N/A
Sirt2 <sup>-/-</sup> OT-II mice	This paper	N/A
<b>Recombinant DNA</b>		
Sirt2 (Myc-DDK-tagged) – Mouse	Origene Technologies Inc	MR225715
pLenti-C-mGFP-P2A-Puro, Lenti	Origene Technologies Inc	PS100093
pLenti-C-Sirt2-mGFP-P2A-Puro, Lenti	This paper	N/A
Lenti-vpak packaging kit	Origene Technologies Inc	TR30037

(Continued on next page)

**Continued**

REAGENT or RESOURCE	SOURCE	IDENTIFIER
Software and Algorithms		
FlowJo software Version 10.0	FlowJo, LLC	<a href="https://www.flowjo.com/">https://www.flowjo.com/</a>
GraphPad Prism 7.0	GraphPad	<a href="https://www.graphpad.com/">https://www.graphpad.com/</a>
ImageJ	N/A	<a href="https://imagej.nih.gov/ij/download.html">https://imagej.nih.gov/ij/download.html</a>
MetaboAnalyst 4.0	N/A	<a href="https://www.metaboanalyst.ca/">https://www.metaboanalyst.ca/</a>
Cluster 3.0	N/A	<a href="http://bonsai.hgc.jp/~mdehoon/software/cluster/software.htm">http://bonsai.hgc.jp/~mdehoon/software/cluster/software.htm</a>
Java TreeView 1.1.6R4.	N/A	<a href="https://sourceforge.net/projects/jtreeview/">https://sourceforge.net/projects/jtreeview/</a>

**RESOURCE AVAILABILITY**

**Lead Contact**

Further information and requests for resources and reagents should be directed to and will be fulfilled by the Lead Contact, Dr. Sung-june Kim ([Sungjune.Kim@Moffitt.org](mailto:Sungjune.Kim@Moffitt.org)).

**Materials Availability**

All materials generated in this study are available from the Lead Contact.

**Data and Code Availability**

The RNA-sequencing dataset generated during this study have been submitted in the Gene Expression Omnibus under the accession number GSE151421. The mass spectrometry proteomics datasets have been deposited to the ProteomeXchange Consortium via the PRIDE ([Vizcaíno et al., 2014](https://www.ebi.ac.uk/pride/)) partner repository with the dataset identifier PXD012811 for the global Sirt2 interacting proteins, PXD012796 for the quantification of lysine acetylation and PXD020150 for the quantification of metabolic Sirt2-interacting proteins in  $T_N$  cells, activated T cells and  $T_M$  cells. Metabolomic datasets have been deposited in MetaboLights database ([Haug et al., 2020](https://www.ebi.ac.uk/metabolights/)) with the accession code MTBLS1795 for the untargeted metabolomic dataset and MTBLS1832 for the targeted Acyl-Carnitines and Acyl-CoA dataset that support the findings of this study.

**EXPERIMENTAL MODEL AND SUBJECT DETAILS**

**Mice**

C57BL/6J mice, Pmel mice with gp100-reactive TCR: B6.Cg-*Thy1*<sup>tg</sup>/Cy Tg(TcraTcrb)8Rest/J, OT-II mice with MHC II-restricted OVA-specific TCR: B6.Cg-Tg(TcraTcrb)425Cbn/J, Sirt2<sup>-/-</sup> mice: B6.129-Sirt2<sup>tm1.1Fwa</sup>/J and NSG mice: NOD.Cg-*Prkdc*<sup>scid</sup> *Il2rg*<sup>tm1Wjl</sup>/SzJ were purchased from The Jackson Laboratory. Pmel mice and OT-II mice were crossed with Sirt2<sup>-/-</sup> mice to generate Sirt2<sup>-/-</sup> Pmel mice and Sirt2<sup>-/-</sup> OT-II mice, respectively. All mice were bred and maintained under specific pathogen-free conditions at the animal facility of H. Lee Moffitt Cancer Center. All animal protocols were approved by the Institutional Animal Care and Use Committee (IACUC). Mice were used at 7–8 weeks of age with age- and sex-matched controls.

**Mouse T Cell Culture**

Spleens and lymph nodes collected from WT, Sirt2<sup>-/-</sup>, WT Pmel, Sirt2<sup>-/-</sup> Pmel, WT OT-II or Sirt2<sup>-/-</sup> OT-II mice were processed into single-cell suspensions. CD3<sup>+</sup>, CD4<sup>+</sup> and CD8<sup>+</sup> T cells were negatively enriched using Mouse Pan T cell, CD4<sup>+</sup> T cell and CD8<sup>+</sup> T cell isolation kits<sup>TM</sup> (Miltenyi Biotec), respectively according to the manufacturer's instructions. The purity of the isolated cells was confirmed by flow cytometry (>95%). Purified T cells were cultured in complete RPMI 1640 medium (Thermo Fisher Scientific) supplemented with 10% fetal bovine serum (FBS, Biowest) and 1% penicillin/streptomycin (P/S, Thomas Scientific Inc.). WT and Sirt2<sup>-/-</sup> T cells were activated with anti-CD3 antibody coated plate (5 µg/ml, 145-2C11, BioXCell) for the indicated time periods. WT Pmel and Sirt2<sup>-/-</sup> Pmel T cells were stimulated with gp100<sub>25-33</sub> (1 µg/ml, AnaSpec) for the indicated time periods. WT OT-II and Sirt2<sup>-/-</sup> OT-II T cells were stimulated with OVA<sub>323-339</sub> peptide (10 µg/ml, InvivoGen) for the indicated time periods.

**Memory Differentiation**

Pmel and OT-II splenocytes were activated with 1 µg/ml gp100<sub>25-33</sub> (AnaSpec) and 10 µg/ml OVA<sub>323-339</sub> (InvivoGen) respectively for 3 days and subsequently cultured in the presence of 10 ng/ml IL-15 (R&D) for 4 days to generate  $T_M$  cells *ex vivo*.

**Human PBMC**

Human PBMC were obtained from healthy donors (OneBlood) by density gradient centrifugation using Ficoll-Paque<sup>TM</sup> PLUS Media (GE Healthcare). CD3<sup>+</sup> T cells were negatively enriched using a human Pan T cell isolation kit<sup>TM</sup> (Miltenyi Biotec). Enriched CD3<sup>+</sup>

T cells were cultured in complete RPMI medium and activated with anti-CD3 antibody coated plate (5  $\mu$ g/ml, OKT-3, BioXCell) in the presence of DMSO (vehicle) or the indicated concentrations of AGK2 and Thiomyristoyl (Selleck Chemicals).

### Human TILs

Human TILs were isolated from tumor biopsies of patients with advanced NSCLC. Collection and expansion of human TILs were approved by an Institutional Review Board protocol. All human samples provided were and remained de-identified. The cohort characteristics including 11 patients enrolled into a phase I clinical trial of Nivolumab and TIL therapy are as previously described (Creelan et al., 2018).

For *ex vivo* expansion, TILs were cultured in complete RPMI 1640 medium, supplemented with 10% human AB serum (Valley Biomedical, Inc.), 1 mM HEPES (Sigma-Aldrich), 1% P/S (Thomas Scientific), 50  $\mu$ g/ml gentamicin (Thermo Fisher Scientific), 50  $\mu$ M  $\beta$ -mercaptoethanol (Thermo Fisher Scientific) and 6,000 U/ml of recombinant human rhIL-2 (PeproTech). For metabolic and functional assays, TILs were cultured in complete RPMI medium, rhIL-2 free, on anti-CD3 antibody coated plate (5  $\mu$ g/ml, OKT-3, BioXCell) in the presence of vehicle or the indicated concentrations of AGK2 (Selleck Chemicals).

### Cell Lines

B16F10 murine melanoma cells, LLC murine lung cancer cells and 293T human embryonic kidney cells were obtained from the American Type Culture Collection (ATCC). Cells were passaged minimally and maintained in complete Dulbecco's Modified Eagle Medium DMEM/F12 (Thermo Fisher Scientific) containing 10% FBS (Biowest) and 1% P/S (Thomas Scientific Inc). B16F10 and LLC cells were used in mouse tumor models. 293T cells were used to generate lentivectors.

## METHOD DETAILS

### Melanoma Lung Metastasis Model

Mice were injected i.v. into lateral tail veins with  $2.5 \times 10^5$  B16F10 tumor cells. For anti-PD-1 administration, mice were injected intraperitoneally (i.p.) with 200  $\mu$ g of anti-PD-1 antibody (RMP1-14, BioXCell) every 3 days for a total of three injections. The number of visible black metastatic nodules on the lung surface was manually counted 18-days post-tumor injection.

### Subcutaneous Tumor Models

Anesthetized mice were injected s.c. into the hind limb with  $2.5 \times 10^5$  B16F10 or LLC tumor cells. Tumor volumes were monitored twice a week over 3 weeks and were calculated using the following equation:  $Volume = length \times width \times height \times \frac{\pi}{6}$ .

### Isolation of Mouse TILs

Lymphocytes from s.c. tumors were isolated by dicing the tissues followed by enzymatic digestion in PBS containing collagenase type 4 (2 mg/ml, Worthington Biochemical) and DNase I (0.25 mg/ml, Sigma-Aldrich) for 45 min with occasional shaking at 37 °C. Cell suspensions were successively filtered through 100  $\mu$ m and 40  $\mu$ m cell strainers (Thermo Fisher Scientific) to obtain single-cell suspension followed by a PBS wash and red blood cell lysis using RBC Lysis Buffer (Biolegend). TILs were finally isolated by density gradient centrifugation using Percoll (GE Healthcare) and were further purified using a CD3 $\epsilon$  MicroBeads kit™ (Miltenyi Biotec) according to the manufacturer's instructions. T cell purity was greater than 90% (data not shown). Fresh TILs were used directly for phenotypic and metabolic analyses or were cultured in complete RPMI medium for functional assays.

### Construction and Production of Lentivectors

The mouse Sirt2 open reading frame was cloned from the pCMV6-Sirt2 expressing vector (Origene) into the pLenti-C-mGFP-P2A-Puro Tagged Cloning Vector (Origene). Lentivectors were generated using Lenti-vpak Packaging Kit (Origene) by transfecting 293T cells with the lentiviral packaging plasmids and either pLenti-Sirt2 plasmids or p-Lenti-Empty plasmids. Viral supernatants were collected 48 and 72 hr after transfection, spun at 3000 rpm for 10 min and filtered through 0.45-mm filters. Lentivectors were finally concentrated using Lenti-X™ Concentrator (Takara Bio) according to the manufacturer's instructions (Clontech).

### Lentivector Transduction

Enriched CD3<sup>+</sup> WT and Sirt2<sup>-/-</sup> T cells were stimulated for 24 hr in anti-CD3 antibody coated plate (5  $\mu$ g/ml, 145-2C11, BioXCell). Freshly concentrated lentivectors were spun-inoculated into activated T cells supplemented with polybrene (6 mg/ml, Sigma) at 2000 rpm, 32 °C for 2 hr.

### In Vivo T Cell Depletion

*In vivo* depletion of CD4<sup>+</sup> or CD8<sup>+</sup> T cell subsets was performed by i.p. injection of 100  $\mu$ g of purified monoclonal anti-CD4 (GK1.5, BioXCell) or anti-CD8 (2.43, BioXCell) antibodies twice weekly. Control (non-depleted) mice were treated with i.p. injection of 100  $\mu$ g of nonimmune IgG isotype control (LTF-2, BioXCell). Depleted and control mice received i.v.  $2.5 \times 10^5$  B16F10 cells (n = 5 per group). The number of visible black metastatic nodules on the lung surface was manually counted 18-days post-tumor injection.

### Adoptive Transfer of Pmel T Cells

In Figure 7E, CD8<sup>+</sup> T cells were purified from spleens of WT Pmel and Sirt2<sup>-/-</sup> Pmel donor mice using CD8<sup>+</sup> T Cell Isolation kit™ (Miltenyi Biotec). NSG mice (n = 8 per group) were injected i.v. with 1 × 10<sup>5</sup> B16F10 melanoma cells. Concurrently, 5 × 10<sup>5</sup> CD8<sup>+</sup> WT Pmel or Sirt2<sup>-/-</sup> Pmel T cells were adoptively transferred into the recipient mice. Control mice received B16F10 tumor cells only. The number of visible black metastatic nodules on the lung surface was manually counted 18-days post-tumor injection. In Figure 7K, Sirt2<sup>-/-</sup> vs. WT Pmel T cells were treated with vehicle or 2 mM 2-DG (Sigma) or 100 nM Oligo (Sigma) for 48 hr. NSG mice (n = 6–8 per group) were injected i.v. with 1.5 × 10<sup>5</sup> B16F10 melanoma cells. Concurrently, 1 × 10<sup>6</sup> of WT vs. Sirt2<sup>-/-</sup> CD8<sup>+</sup> Pmel untreated T cells or 2-DG- or Oligo-treated T cells were adoptively transferred into the recipient mice. Control mice received B16F10 tumor cells only. The number of visible black metastatic nodules on the lung surface was manually counted 15-days post-tumor injection.

### Flow Cytometry

For analysis of surface markers, mouse T cells were stained in PBS containing 5% FBS (FACS buffer) with: CD3 (BUV395), CD4 (BUV805), PD-1 (BV605), Gr1 (BUV395), F4/80 (BV711), CD19 (PerCP-Cy5.5), NK1.1 (PE) from BD Biosciences, CD8 (Alexa Fluor 700), CD44 (Alexa Fluor 488), CD62L (PE-Cy7), CD27 (BV 510), CD11b (BV605), CD11c (Alexa488), IA/IE (Alexa647), B220 (APC-H7) from Biolegend, PBS57-loaded CD1d tetramer (Alexa647) from NIH Tetramer Facility, and glucose transporter GLUT1 (Alexa647) from Abcam, incubated at 4 °C for 1 hr, then washed twice with FACS buffer, and finally fixed in PBS containing 1% paraformaldehyde. For human T cells staining the following antibodies were used instead: CD8 (BUV395), CD3 (BUV496), CD4 (BUV737), and CD45RA (FITC) from BD Biosciences. Dead cells were excluded using the Zombie Violet or Zombie NIR Fixable Viability Kit (Biolegend) following the manufacturer's protocol. Frequencies of apoptotic cells were quantified using APC-labeled Annexin V and DAPI staining according to manufacturer's instructions (Invitrogen). For glucose uptake, the fluorescent glucose analog 2-NBDG (Thermo Fisher Scientific) was added to the cells at 10 μM for 1 hr prior cell surface staining. MitoTracker Green staining was performed according to the manufacturer's instructions (Invitrogen).

For Sirt2 and KI-67 intracellular staining, cells were first labeled with surface markers before fixation/permeabilization with BD Pharmingen™ Transcription Factor Kit (BD Biosciences) and then stained with Sirt2 antibody (Sigma-Aldrich, #9441) combined with a secondary goat anti-rabbit IgG antibody (Alexa647, Thermo Fisher Scientific) or KI-67 (APC, Biolegend).

For cytokine intracellular staining, cells were first re-stimulated with phorbol 12-myristate 13-acetate (PMA, 10 ng/ml, Sigma-Aldrich) and ionomycin (1 μM, Sigma-Aldrich) for 1 hr followed by GolgiPlug™ treatment (1%, BD Biosciences) for additional 6 hr. Cells were then surface stained before fixation/permeabilization with Cytotfix/Cytoperm™ Kit (BD Biosciences), followed finally by TNF-α (FITC, Biolegend), IFN-γ (BV711, BD Biosciences) and granzyme B (Alexa647, Biolegend) staining.

Cells were acquired on a BD FACSymphony™ A5 and LSR II (Becton Dickinson), and data were analyzed with FlowJo Version 10.0 software.

### CFSE Dilution Assay

Pmel T cells were first labeled with 5 μM of CellTrace™ carboxyl fluorescein succinimidyl ester (CFSE, Thermo Fisher Scientific) for 30 min at room temperature (RT) and then stimulated with gp100 or remained non-stimulated for 3–4 days. Murine TILs freshly isolated from s.c. B16F10 tumor nodules were labelled with 5 μM CFSE for 30 min at RT and then co-cultured with irradiated B16F10 cells for 3 days.

### Enzyme-Linked Immunospot (ELISPOT) Assay

The number of IFN-γ producing cells was evaluated in an ELISPOT assay. Briefly, mouse TILs were plated at 1 × 10<sup>5</sup> cells and co-cultured with 1 × 10<sup>5</sup> irradiated B16F10 tumor cells (50 Gray) in the presence of the indicated concentrations of 2-DG (Sigma-Aldrich), in a 96-well nitrocellulose flat-bottomed plate (ELISPOT plate, Millipore) pre-coated with anti-mouse IFN-γ antibody (AN-18, Mabtech, Inc.) and incubated for 48 hr at 37°C. For Pmel T cells, splenocytes were first stimulated with gp100 (1 μg/ml, Anaspec) for 48 hr in the presence of the indicated concentrations of 2-DG (Sigma-Aldrich) and then transferred to the ELISPOT plate pre-coated with anti-mouse IFN-γ antibody (AN-18, Mabtech, Inc.) for an additional 48 hr. For human CD3<sup>+</sup> T cells and TILs, cells were first stimulated with plate-coated anti-CD3 for 48 hr in the presence of vehicle, AGK2 or TM at the indicated concentration and then transferred to the ELISPOT plate pre-coated with anti-human IFN-γ antibody (1-D1K, Mabtech, Inc.). PMA (10 ng/ml, Sigma-Aldrich) was used as positive assay control. After washing steps and successive biotinylated anti-IFN-γ antibody (R4-6A2, Mabtech, Inc.) and Streptavidin-HRP (BD Bioscience) labeling, spots were detected using AEC Substrate Kit (BD Biosciences) and counted using an AID ELISPOT Reader System (Autoimmun Diagnostika GmbH).

### Lactate Dehydrogenase (LDH) Release Assay

Evaluation of functional cytotoxic activity was performed using Pierce™ LDH Cytotoxicity Assay Kit (Thermo Fisher Scientific) according to the manufacturer's protocol. B16F10 cells or human NSCLC tumor cells were used as target cells. Mouse CD3<sup>+</sup> TILs isolated from s.c. B16F10 tumors or CD8<sup>+</sup> enriched T cells from gp100-stimulated Pmel splenocytes or autologous human NSCLC TILs were used as effector cells. Target tumor cells were co-cultured with effector cells in 96-well round-bottom microplates at the indicated effector:target ratios with and without the indicated inhibitors. After 6 hr, the percentage of specific LDH release was calculated according to the following formula:

$$\text{Cytotoxicity \%} = \frac{\text{experimental value} - \text{effectors spontaneous release} - \text{targets spontaneous release}}{\text{target cells maximum release} - \text{target cells spontaneous release}} \times 100$$

where “experimental” corresponds to the experimental signal value, “effector spontaneous” to spontaneous release of LDH from effector cells alone, “target spontaneous” to spontaneous release of LDH from target cells alone and “maximum release” to the maximum release of LDH from target cells in medium containing 1% Triton X-100.

### Extracellular Flux Analysis

Extracellular acidification rate (ECAR), proton efflux rate (PER) and oxygen consumption rate (OCR) were measured using the Seahorse XF analyzer (Agilent technologies). Glycolysis Stress Test (GST), glycolytic rate assay (GRA) and mitochondrial stress test (MST) were purchased from Agilent technologies and performed according to the kit manufacturer’s instructions.

The day of the assay,  $2 \times 10^5$  activated T cells were plated in Cell-Tak (Corning)-coated XF96 plates in XF media (XF RPMI Medium pH 7.4 containing 2 mM L-glutamine only for GST or supplemented with 10 mM glucose, 2 mM L-glutamine and 1 mM sodium pyruvate for GRA and MST, all from Agilent technologies) via centrifugation to ensure cell attachment. Cells were equilibrated for 1 hr in a non-CO<sub>2</sub> incubator before starting the assay.

For GST, ECAR and OCR were measured under basal conditions and in response to 10-mM glucose, 1  $\mu$ M Oligo and 50 mM 2-DG successively to calculate basal glycolytic rate, glycolytic capacity (in response to Oligo), and glycolytic reserve (= *glycolytic capacity* – *basal rate*).

For GRA, PER and OCR were measured under basal conditions and in response to 0.5  $\mu$ M rotenone/antimycin A (R/A) and 50 mM 2-DG successively to calculate basal glycolysis and compensatory glycolysis (in response to R/A).

For MST, OCR and ECAR were measured under basal conditions and in response to sequential injections of 1  $\mu$ M Oligo, 1  $\mu$ M FCCP (Carbonyl cyanide 4-trifluoromethoxyphenylhydrazone) and 0.5  $\mu$ M R/A to calculate basal respiration rate (= *baseline OCR* – *R/A OCR*), maximal respiration rate (= *FCCP OCR* – *R/A OCR*), and oxidative reserve (= *maximal respiration* – *basal respiration*).

To measure the contribution of glycolysis, glutaminolysis and FAO as fuels for mitochondrial metabolism, OCR and ECAR were measured under basal conditions and in response to sequential injections of vehicle, UK5099 (2  $\mu$ M), BPTES (3  $\mu$ M) or Etomoxir (4  $\mu$ M) inhibitors and then 1  $\mu$ M Oligo, 1  $\mu$ M FCCP and 0.5  $\mu$ M R/A.

To measure oxidation of exogenous and endogenous FA, T cells were activated in complete RPMI media for 3 days and transferred to substrate-limited media overnight. Substrate limited media contained 0.5 mM glucose, 1 mM glutamine, 0.5 mM carnitine (all from Sigma) and 1% FBS (Biowest). Palmitate or BSA substrates were added immediately before the assay. OCR was measured under basal conditions and in response to sequential injections of vehicle, or Etomoxir (4  $\mu$ M) and then 1  $\mu$ M Oligo, 1  $\mu$ M FCCP and 0.5  $\mu$ M R/A. The relative contribution of FAO to OCR was calculated as follows:

$$\text{Exogenous FA oxidation} = \text{Maximal Palmitate} + \text{vehicle OCR} - \text{maximal BSA} + \text{vehicle OCR} - \text{OCR due to uncoupling by free FA}$$

$$\text{Uncoupling by free FA} = \text{Palmitate} + \text{vehicle OCR after Oligo injection} - \text{BSA} + \text{vehicle OCR after Oligo injection}$$

$$\text{Endogenous FA oxidation} = \text{Maximal BSA} + \text{vehicle OCR} - \text{maximal BSA} + \text{Etomoxir OCR}$$

Results were normalized to total protein quantified using Pierce™ BCA Protein Assay Kit (Thermo Fisher Scientific).

### Enzyme Activity Assay

WT and Sirt2<sup>-/-</sup> CD3<sup>+</sup> enriched T cells were activated on anti-CD3 antibody-coated plates for 3 days. Enzymatic activities of aldolase, enolase, GAPDH, hexokinase, phosphofruktokinase, aconitase, oxoglutarate dehydrogenase, succinate dehydrogenase and succinyl-CoA ligase were measured on T cells lysates using an enzymatic colorimetric assay kit (all from Biovision) according to the manufacturer’s instructions.

### Lactate, Glutamine, and Glutamate Measurement

Extracellular lactate, glutamine and glutamate concentrations were determined using the YSI 2900 Biochemistry Analyzer (YSI Incorporated). Briefly,  $2 \times 10^6$  CD3<sup>+</sup> enriched T cells were cultured in three separate 2 ml fresh media on anti-CD3 antibody coated wells. Three days post-activation, cell culture supernatants were harvested for metabolite quantitation. All assays were performed in triplicate with results normalized to the Calibrator Standard (YSI Incorporated) and compared to fresh media.

### ADP/ATP Ratio Assay

The intracellular ATP/ADP level was measured using ADP/ATP Ratio Assay Kit (Sigma-Aldrich), based on bioluminescence detection reaction according to the manufacturer’s instructions. CD3<sup>+</sup> enriched T cells were plated in anti-CD3 coated 96-well microplate. Three days post-activation, cells were lysed in nucleotide-releasing buffer. ATP and ADP levels were determined by measuring bioluminescent intensities in the presence and the absence of ADP converting enzyme successively using a multi-mode microplate reader (Synergy HTX, BioTek).

### Immunoprecipitation

For immunoprecipitation (IP) assays, activated CD3<sup>+</sup> T cells were lysed in IP lysis buffer (20 mM HEPES, pH 7.9, 180 mM KCl, 0.2 mM EDTA, 1.5 mM MgCl<sub>2</sub>, 20% glycerol, 0.1% Nonidet P-40, containing a mixture of protease inhibitors). Cell lysates were incubated overnight at 4 °C with specific antibodies against Sirt2 (#S8447, 1:50) from Sigma-Aldrich, acetyl-lysine (#9441, 1:50), ENO1 (#3810, 1:50), ALDOA (#8060, 1:50), PKM1/2 (#3106, 1:50), OGDH (#26865, 1:50), ACO2 (#6571, 1:50), SDHA (#11998, 1:50) and SUCLG1 (#8071, 1:50) from Cell Signaling, GAPDH (#ab181602, 1:60), LDH (#ab52488, 1:30), PFKP (#ab204131, 1:80) from Abcam, HK1 (#NBP2-67503, 1:50) or PGK1 (#NBP2-67534, 1:50) from Novus biologicals. Rabbit monoclonal antibody IgG (Cell Signaling, #3900) was used as an isotype control. After addition of anti-rabbit Ig agarose-beads (TrueBlot®, Rockland), samples were incubated at 4 °C for 2 hr. Beads were washed five times with IP lysis buffer and proteins were released from the beads by boiling in 3X SDS sample loading buffer and loaded into 10 % SDS-PAGE gel for WB analysis.

### Western Blot Analysis

Whole cell lysates were prepared using lysis buffer (Pierce RIPA buffer, Thermo Fisher Scientific) supplemented with cComplete™ protease inhibitor cocktail and PhosSTOP phosphatase inhibitor cocktail (Roche Applied Science).

Cell lysates (20 µg) or IP samples were loaded onto 10% SDS-PAGE and separated by electrophoresis followed by semi-dry transfer into polyvinylidene fluoride membranes (Immun-Blot® PVDF membrane, Bio-Rad) using Trans-Blot Turbo transfer system (Bio-Rad). After transfer, the membranes were blocked at RT with Tris-buffered saline (TBS) containing 0.05% Tween-20 (TBST) and 5% non-fat dry milk for 1 hr and then incubated overnight at 4 °C with specific primary antibodies (indicated below). The membranes were washed three times with TBST and then incubated for 1 hr with horseradish peroxidase (HRP)-conjugated goat anti-mouse IgG H&L (Abcam, #ab97051, 1:3,000) for regular WB analysis, or HRP-conjugated mouse anti-rabbit IgG light-chain specific (Cell Signaling, #93702, 1:1,000) for IP samples. After 3 washes with TBST, bound antibodies were detected by chemiluminescence using the Pierce™ ECL Western Blotting Substrate and the Super Signal West Femto Maximum Sensitivity Substrate kits (Thermo Fisher Scientific). Image acquisition was performed with the Amersham imager 600 system (GE Healthcare Bio-Sciences).

Immunoblotting was performed using primary antibodies against: acetyl-lysine (#9441, 1:1,000), ENO1 (#3810, 1:1,000), acetylated-tubulin (#5335, 1:1,000),  $\alpha$ -tubulin (#2144, 1:1,000) ALDOA (#8060, 1:1,000), PKM1/2 (#3106, 1:1,000), OGDH (#26865, 1:1,000), ACO2 (#6571, 1:1,000), SDHA (#11998, 1:1,000), SUCLG1 (#8071, 1:1,000), ASCT2 (#5345, 1:1,000), c-Myc (#9402, 1:1,000) and P-S6 (#4858, 1:2,000) from Cell Signaling,  $\beta$ -Actin (#ab8227, 1:5,000), Sirt2 (#ab67299, 1:200), GAPDH (#ab181602, 1:10,000), LDH (#ab52488, 1:5,000), PFKP (#ab204131, 1:2,000), HK1 (#ab150423, 1:1,000), CPT1 $\alpha$  (#ab128568, 1:1,000), HADHA (#ab203114, 1:2,000), HADHB (#ab240601, 1:2,000), GLS (#ab202027, 1:1,000) and HIF-1 $\alpha$  (#ab82832, 1:1,000) from Abcam and PGK1 (#NBP2-67534, 1:1,000) from Novus biologicals.

### Transmission Electron Microscopy

TEM analysis was performed at the Lisa Muma Weitz Microscopy Core, University of South Florida.

WT vs. Sirt2<sup>-/-</sup> CD4<sup>+</sup> OT-II T cells at naïve, activated and memory stages, were fixed with 2.5% glutaraldehyde in 0.1M phosphate buffer (Electron Microscopy Sciences, EMS). Following fixation, samples were washed in 0.2M cacodylate buffer and post fixed in 1% osmium tetroxide (EMS). After brief washing in distilled H<sub>2</sub>O, samples were dehydrated in increasing ethanol concentrations and incubated in three changes of EMBED 812 resin (EMS) before a final embedding. After curing, cut sections of 90 nm were collected on copper grids and stained with 2% aqueous uranyl acetate and lead citrate (EMS). Images were obtained using a JEOL 1400 transmission electron microscope equipped with side mounted Orius digital camera (Gatan).

### RNA-Sequencing Analysis

RNA-sequencing analysis was performed at the Molecular Genomics Core Facility of H. Lee Moffitt Cancer Center.

WT and Sirt2<sup>-/-</sup> CD4<sup>+</sup> T cells were stimulated with anti-CD3 plate-coated for 24 hr or remained unstimulated (n = 3 per group). RNA was extracted using the RNeasy Mini Kit (Qiagen; cat. #74106) and processed for RNA-sequencing using the NuGen Ovation Mouse RNA-Seq System (NuGen Inc). Briefly, 100 ng of RNA was used to generate cDNA and a strand-specific library following the manufacturer's protocol. Quality control steps including TapeStation library assessment and quantitative RT-PCR for library quantification were performed. The libraries were sequenced on the Illumina NextSeq 500 sequencer with 2 × 75-base paired-end high output runs in order to generate 30 million read pairs per sample.

### Liquid Chromatography-Tandem Mass Spectrometry (LC-MS/MS)

LC-MS/MS analysis was performed at the Proteomics and Metabolomics Core Facility of H. Lee Moffitt Cancer Center.

For the identification of Sirt2 interacting targets, CD3<sup>+</sup> T cells were cultured on anti-CD3 coated-plates for 24 hr, washed with PBS and lysed in the IP lysis buffer. To quantify Sirt2 interactome in different T cell subsets, CD3<sup>+</sup> purified T cells were cultured on anti-CD3 coated-plates for 48 hr, washed with PBS and lysed in the IP lysis buffer; and CD4<sup>+</sup> OT-II T<sub>M</sub> cells were generated as described above, washed with PBS and lysed in the IP lysis buffer. Unstimulated CD3<sup>+</sup> T<sub>N</sub> cells and CD4<sup>+</sup> OT-II T<sub>N</sub> cells were directly washed with PBS and lysed in the IP lysis buffer following their isolation from spleens.

Immunoprecipitation assay was performed as described previously using Anti-Sirt2 Abs (Sigma-Aldrich) vs. isotype control Abs (Cell Signaling). The immune-precipitated proteins were loaded onto 10% SDS-PAGE and separated by electrophoresis. The gel bands were excised and proteins were reduced with Tris (2-carboxy-ethyl) phosphine hydrochloride (TCEP), followed by alkylation

with iodoacetamide. In-gel digestion with trypsin was carried out at 37 °C overnight. Ziptip C18 micropipette columns were used to desalt the tryptic peptides.

For identification of acetylated proteins, WT and Sirt2<sup>-/-</sup> CD3<sup>+</sup> purified T cells were cultured on anti-CD3 coated-plates for 72 hr, washed with PBS and lysed in denaturing lysis buffer containing 8 M urea, 20 mM HEPES (pH 8), 1 mM sodium orthovanadate, 2.5 mM sodium pyrophosphate and 1 mM β-glycerophosphate. A Bradford assay was performed to determine the protein concentration. Equal amounts of total protein were analyzed for each sample. The mixed proteins were reduced with 4.5 mM DTT and alkylated with 10 mM iodoacetamide. Trypsin digestion was carried out at RT overnight, and tryptic peptides were then acidified with 1% trifluoroacetic acid (TFA) and desalted with C18 Sep-Pak cartridges according to the manufacturer's instructions.

Following lyophilization, the dried peptide pellet was re-dissolved in IAP buffer containing 50 mM MOPS pH 7.2, 10 mM sodium phosphate and 50 mM sodium chloride. Acetyl-lysine-containing peptides were immuno-precipitated with immobilized bead-conjugated anti-acetyl-lysine (#13416, Cell Signaling). After 2 hr incubation, the antibody-beads were washed 3 times with IAP buffer, followed by 2 washes with H<sub>2</sub>O. The acetyl-lysine peptides were eluted twice with 0.15% TFA, and the volume was reduced to 20 μl via vacuum centrifugation. The eluted peptides were fractionated using Pierce High pH Reversed-Phase Peptide Fractionation Kit (Thermo Fisher Scientific).

A nanoflow ultra high performance liquid chromatograph (RSLC, Dionex) coupled to an electrospray bench top orbitrap mass spectrometer (Q Exactive Plus, Thermo Fisher Scientific) was used for tandem mass spectrometry peptide sequencing experiments. The sample was first loaded onto a pre-column (100 μm ID × 2 cm in length packed with C18 reversed-phase resin, 5 μm particle size, 100Å pore size) and washed for 8 min with aqueous 2% acetonitrile and 0.04% trifluoroacetic acid. The trapped peptides were eluted onto the analytical column, (C18, 75 μm ID × 25 cm in length, 2 μm particle size, 100Å pore size, Dionex). The 90-minute gradient was programmed as: 95% solvent A (2% acetonitrile + 0.1% formic acid) for 8 min, solvent B (90% acetonitrile + 0.1% formic acid) from 5% to 38.5% in 60 min, then solvent B from 50% to 90% B in 7 min and held at 90% for 5 min, followed by solvent B from 90% to 5% in 1 min and re-equilibration for 10 min. The flow rate on analytical column was 300 nl/min. Sixteen tandem mass spectra were collected in a data-dependent manner following each survey scan using 15 second exclusion for previously sampled peptide peaks.

For data analysis, both MASCOT (Perkins et al., 1999) and SEQUEST (Eng et al., 1994) search algorithms were used to identify proteins from IP samples. The results were summarized in Scaffold (proteomesoftware.com). MaxQuant (Cox and Mann, 2008) (version 1.2.2.5) was used to identify and quantify relative intensities of acetyl-lysine containing peptides.

### Untargeted Metabolomic Analysis

Metabolomic analysis was performed at the Proteomics and Metabolomics Core Facility of H. Lee Moffitt Cancer Center.

CD8<sup>+</sup> purified T cells from WT (n = 5) and Sirt2<sup>-/-</sup> (n = 4) mouse spleens were stimulated in anti-CD3 coated plate for 72 hr followed by extensive washes with PBS. Metabolites were extracted from cells using 80% methanol (pre-cooled at -80 °C at least 1 hr in advance). After 30 min incubation at -80 °C, samples were centrifuged (10 min, 18,800 × g, 4 °C) and supernatants were collected, dried and re-suspended in 80% methanol. The protein pellets were used for protein quantification to serve as a sample quality control.

UHPLC-MS was performed using a Vanquish LC (Thermo Fisher Scientific) interfaced with a Q Exactive HF mass spectrometer (Thermo Fisher Scientific). Chromatographic separation was performed on a SeQuant ZIC-pHILIC LC column (4.6 mm ID × 150 mm in length, 5 μm particle size, Millipore). In order to maintain stable column pressure and further filtering solvents, SeQuant ZIC-pHILIC guard column (4.6 mm × 20 mm in length, 5 μm particle size, Millipore) was connected before the LC column. The mobile phase A was aqueous 10 mM ammonium carbonate and 0.05% ammonium hydroxide (Sigma-Aldrich) using LC-MS grade Water (VWR), and the mobile phase B was 100% acetonitrile (VWR). The total running time was 20 min. The column temperature was set to 30 °C and the injection volume was 2 μl. Separate UHPLC-MS analyses were carried out in the positive and negative ion modes using the mass scan range from m/z 60 to m/z 900. Results were normalized to total protein.

### Acyl-Carnitines, Acyl-CoA and Acetyl-CoA Analysis by LC-MS/MS

CD8<sup>+</sup> purified T cells from WT (n = 5) and Sirt2<sup>-/-</sup> (n = 6) mouse spleens were stimulated in anti-CD3 coated plate for 72 hr, followed by extensive washes with PBS. Metabolites were extracted from cells using 80% methanol (pre-cooled at -80 °C at least 1 hr in advance) containing the corresponding internal standards: L-Carnitine (trimethyl-D<sub>9</sub>), O-Acetyl-L-Carnitine (N-methyl-D<sub>3</sub>), O-Butyryl-L-Carnitine (N-methyl-D<sub>3</sub>), O-Hexanoyl-L-Carnitine (N-methyl-D<sub>3</sub>), O-Octanoyl-L-Carnitine (N-methyl-D<sub>3</sub>), O-Decanoyl-L-Carnitine (N-methyl-D<sub>3</sub>), O-Lauroyl-L-Carnitine (N,N,N-trimethyl-D<sub>3</sub>), O-Myristoyl-L-Carnitine (N,N,N-trimethyl-D<sub>3</sub>), O-Palmitoyl-L-Carnitine (N-methyl-D<sub>3</sub>), O-Stearoyl-L-Carnitine (N-methyl-D<sub>3</sub>), Acetyl-coenzyme A (1,2-<sup>13</sup>C<sub>2</sub>), which were all purchased from Cambridge Isotope Labs. After 30 min incubation at -80 °C the samples were centrifuged (10 min, 18,800 × g, 4 °C) and the supernatants were collected, dried and re-suspended in 80% methanol. The protein pellets were used for protein quantification using Bradford assay to serve as a sample quality control.

UHPLC-MS was performed using a Vanquish LC (Thermo Fisher Scientific) interfaced with a Q Exactive FOCUS mass spectrometer (Thermo Fisher Scientific).

For Acyl-CoA: an AccuCore Vanquish C18+ (2.1 mm × 100 mm, 1.5 μm particle size, Thermo Fisher Scientific) was used for the LC separation; the mobile phase A was 10:90 acetonitrile: water with 15 mM ammonium hydroxide, and the mobile phase B was 100% acetonitrile with 15 mM ammonium hydroxide. The total running time was 15 min and Parallel Reaction Monitoring (PRM) was performed in positive mode.

For Acetyl-CoA: an AccuCore C18 column (2.1 mm × 100 mm, 2.6 μm particle size, Thermo Fisher Scientific) was used; the mobile phase A was 5mM dibutyl ammonium acetate (Sigma-Aldrich) and ammonium acetate pH = 9.0 (Sigma-Aldrich), and the mobile phase B was 100% methanol with 0.1% formic acid. The total running time was 9 min and full MS<sup>1</sup> was performed in negative mode.

For all analyses the column temperature was set to 30°C with an injection volume of 2 μL. Peak heights were determined using Skyline (version 19.1). For Acyl Carnitines and Acetyl CoA the amounts (in μg) were calculated using the peak height ratio of each molecule to its respective internal standard. For Acyl CoA, only the peak heights obtained from Skyline were reported due to the unavailability of internal standards during the analysis.

### Enrichment Analysis

For gene set enrichment analysis, the list of upregulated genes in Sirt2<sup>-/-</sup> T cells vs. WT T cells was uploaded to MSigDB (Subramanian et al., 2005) and the overlap with the HALLMARK gene sets was calculated (Liberzon et al., 2015). A false discovery rate q-value < 0.001 was used as cut-off.

For metabolite set enrichment analysis (MSEA), the list of increased metabolites in Sirt2<sup>-/-</sup> vs. WT T cells was submitted into the MSEA web-based tool (<https://www.metaboanalyst.ca/>), that is incorporated into MetaboAnalyst 4.0 platform (Xia and Wishart, 2010). Overrepresentation analysis was the selected enrichment analysis method. The overlap with pathway-associated metabolites set library was implemented using the hyper-geometric test. One-tailed *P* values were provided after adjusting for multiple testing. A false discovery rate q-value < 0.15 was used as cut-off.

### QUANTIFICATION AND STATISTICAL ANALYSIS

Statistical analyses were performed with Prism software version 7.01 (GraphPad Software) using two-tailed unpaired or paired Student's t-test and one- or two-way ANOVA. In all cases, statistical significance was considered when  $p < 0.05$ . Error bars show mean ± standard error of the mean (SEM) and *p* values were represented as follows:  $p < 0.05$ , \*\* $p < 0.01$ , \*\*\* $p < 0.001$ , \*\*\*\* $p < 0.0001$ .